Mon. Not. R. Astron. Soc. **377,** 1301–1323 (2007) doi:10.1111/j.1365-2966.2007.11691.x

Open clusters in dense fields: the importance of field-star decontamination for NGC 5715, Lyngå 4, Lyngå 9, Trumpler 23, Trumpler 26 and Czernik 37

C. Bonatto★ and E. Bica

Departamento de Astronomia, Universidade Federal do Rio Grande do Sul, Av. Bento Gonçalves 9500, Porto Alegre 91501-970, RS, Brazil

Accepted 2007 March 1. Received 2007 February 28; in original form 2006 November 13

ABSTRACT

Star clusters projected on to dense stellar fields in general require field-star (FS) decontamination to confirm their nature and derive intrinsic photometric and structural fundamental parameters. This work focuses on the open clusters (OCs) or candidates NGC 5715, Lyngå 4, Lyngå 9, Trumpler 23, Trumpler 26 and Czernik 37 which are projected within $317^\circ \lesssim \ell \lesssim 2^\circ.2$ and $|b| \lesssim 2^\circ.8$, against crowded bulge and/or disc fields. To tackle these difficult objects we develop a colour–magnitude diagram FS-decontamination algorithm based on 2MASS J, $(J - H)$ and $(J - K_s)$ data, and respective uncertainties, to detect cluster star excesses over the background. On the other hand, colour–magnitude filters are used to build stellar radial density profiles and mass functions. The results convey compelling evidence that Lyngå 9 and Czernik 37 are intermediate-age OCs, and their fundamental parameters are measured for the first time. Trumpler 23 is a particularly challenging object, since besides high background level, its field presents variable absorption in near-infrared bands. We confirm it to be an intermediate-age OC. Trumpler 26 is studied in more detail than in previous works, while NGC 5715 and Lyngå 4 have fundamental parameters determined for the first time. These OCs are located 0.9–1.6 kpc within the solar circle, with ages similar to that of the Hyades. Structurally, they are well described by King profiles. In all cases, core and limiting radii are significantly smaller than those of nearby OCs outside the solar circle. We test the effect of background levels on cluster radii determinations by means of simulations. They indicate that for central clusters, radii may be underestimated by about 10–20 per cent, which suggests that the small sizes measured for the present sample reflect as well intrinsic properties related to dynamical evolution effects. The objects probably have been suffering important tidal effects that may have accelerated dynamical evolution, especially in Czernik 37, the innermost object.

Key words: open clusters and associations: individual: NGC 5715 – open clusters and associations: individual: Lyngå 4 – open clusters and associations: individual: Lyngå 9 – open clusters and associations: individual: Trumpler 23 – open clusters and associations: individual: Trumpler 26 – open clusters and associations: individual: Czernik 37.

1 INTRODUCTION

Colour–magnitude diagrams (CMDs) of most open clusters (OCs) feature age-dependent stellar sequences such as fractions of the main sequence (MS), turn-off (TO) and giant branch (GB), that provide essential information to derive their reddening, age and distance from the Sun. In this sense, OCs have been used as probes of Galactic disc properties (Lyngå 1982; Janes & Phelps 1994; Friel 1995; Bonatto et al. 2006a; Piskunov et al. 2006).

However, the proximity of most OCs to the plane and the corresponding strong reddening and field-star (FS) contamination, especially for OCs projected against the central parts of the Galaxy, usually restrict this analysis to the more populous OCs and/or those located a few kpc from the Sun (Bonatto et al. 2006a, and references therein). Using a sample of 654 OCs with available fundamental parameters, Bonatto et al. (2006a) found that a large fraction of the intrinsically faint and/or distant OCs must be drowned in the field, particularly in bulge/disc directions. They estimate a total

★E-mail: charles@if.ufrgs.br

population of $\sim 10^5$ OCs in the Galaxy, in agreement with Piskunov et al. (2006).

Because they are minority in catalogues, OCs projected towards the central parts of the Galaxy are of particular interest. Studies like this one can provide means to unambiguously unveil the nature of such potential candidates, which is essential to establish the fraction of star clusters as compared to statistical fluctuations of the dense stellar field in those directions.

Reliable fundamental parameters of unstudied OCs are important both to disc studies and to constrain theories of molecular cloud fragmentation, star formation, as well as stellar and dynamical evolutions. Structural and dynamical-related parameters of star clusters can be used to investigate whether the apparent scarcity of OCs inside the solar circle is due to observational limitations in dense stellar fields or enhanced tidal disruption rates because of proximity to the bulge and/or higher rates of collisions with molecular clouds (Bonatto et al. 2006a, and references therein).

As a first step a series of faint OCs were studied using near-infrared (near-IR) J, H and K_s photometry (Bica, Bonatto & Dutra 2003, 2004; Bica & Bonatto 2005) obtained from the 2MASS[1] Point Source Catalogue (PSC). 2MASS spatial and photometric uniformity has been important to derive fundamental parameters and probe the nature of these objects, because it allows extraction of large surrounding fields that provide high star-count statistics in the near-IR.

To this purpose we have developed quantitative tools to disentangle cluster and FSs in CMDs, in particular two different kinds of filters. Basically we apply (i) FS decontamination to uncover cluster evolutionary sequences from the field, which is important to derive reddening, age and distance from the Sun, and (ii) colour–magnitude (CM) filters, which proved to be essential for building intrinsic stellar radial density profiles (RDPs), as well as luminosity and mass functions (MFs). In particular, FS decontamination constrains more the age and distance from the Sun, especially for low-latitude OCs (Bonatto et al. 2006a). These tools were applied to OCs and embedded clusters to enhance MS and/or pre-MS sequences with respect to the field (Bica & Bonatto 2005; Bonatto & Bica 2005, 2006; Bonatto et al. 2006b; Bonatto, Santos & Bica 2006). They were useful also in the analysis of faint and/or distant OCs (Bica, Bonatto & Dutra 2003, 2004; Bica & Bonatto 2005; Bica, Bonatto & Blumberg 2006). In addition, more constrained structural parameters such as core (King 1966a,b) and limiting radii ($R_{\rm core}$ and $R_{\rm lim}$, respectively), and MF slopes have been derived from CM-filtered photometry, allowing inferences on cluster dynamical state (e.g. Bonatto & Bica 2005).

This work investigates photometric and structural properties of six OCs or candidates in dense stellar fields: NGC 5715, Lyngå 4, Lyngå 9, Trumpler 23, Trumpler 26 and Czernik 37. They were included in early catalogues of star clusters (Alter et al. 1970; Lyngå 1985, and references therein), but only recently some of them have been analysed. From four to six catalogues (columns 1 and 13 of Table 1) considered these objects as OCs or candidates on plate materials. Hereafter, we will adopt the acronyms Ly, Tr and Cz.

The objects are projected within $\approx 45^\circ$ of the Galactic Centre. NGC 5715, Ly 4, Tr 23, Ly 9 and Tr 26 are located in the fourth quadrant while Cz 37 is in the first quadrant. We are dealing with very low latitude objects, all with $|b| \lesssim 2.^\circ 8$. Clearly, they are ideal targets to be analysed with decontamination methods.

[1] The Two-Micron All-Sky Survey, All-Sky data release (Skrutskie et al. 1997), available at http://www.ipac.caltech.edu/2mass/releases/allsky/.

Table 1. Fundamental parameters.

	Measured from XDSS				Present results derived from 2MASS data							
Cluster	α(2000)	δ(2000)	D		α(2000)	δ(2000)	ℓ	b	Age	$E(B-V)$	$D_\odot$	$d_{\rm GC}$	Alternative Names
	($^{\rm h}$ $^{\rm m}$ $^{\rm s}$)	($^\circ$ $'$ $''$)	(arcmin)	($^{\rm h}$ $^{\rm m}$ $^{\rm s}$)	($^\circ$ $'$ $''$)	($^\circ$)	($^\circ$)	(Gyr)		(kpc)	(kpc)		
(1)	(2)	(3)	(4)		(5)	(6)	(7)	(8)	(9)	(10)	(11)	(12)	(13)
NGC 5715	14:43:30	−57:34:37	6		14:43:37.0	−57:34:33.6	317.54	+2.08	0.8 ± 0.1	0.42 ± 0.03	1.5 ± 0.1	6.2 ± 0.1	Mel-128,Cr 286,OCl-929,BH 163,ESO 176SC2
Lyngå 4	15:33:19	−55:14:11	6		15:33:19.0	−55:14:00.0	324.60	+0.66	1.3 ± 0.2	0.70 ± 0.07	1.1 ± 0.1	6.3 ± 0.1	OCl-941,BH 174,ESO 147SC7
Trumpler 23	16:00:49	−53:32:10	5		16:00:46.1	−53:31:26.4	328.85	−0.47	0.9 ± 0.1	0.58 ± 0.03	1.9 ± 0.1	5.7 ± 0.1	Cr 295,OCl-950,BH 180,ESO 178SC6
Lyngå 9	16:20:41	−48:31:44	6		16:20:41.0	−48:32:00.0	334.54	+1.07	0.7 ± 0.1	1.18 ± 0.11	1.7 ± 0.2	5.7 ± 0.2	OCl-966,BH 189,ESO 226SC2
Trumpler 26	17:28:32	−29:29:50	5		17:28:32.0	−29:29:50.0	357.50	+2.84	0.7 ± 0.1	0.35 ± 0.03	1.0 ± 0.1	6.3 ± 0.1	Harvard 15,Cr 331,OCl-1032,ESO 454SC33
Czernik 37	17:53:17	−27:22:10	5		17:53:17.0	−27:22:10.0	2.21	−0.64	0.6 ± 0.1	1.06 ± 0.03	1.7 ± 0.1	5.6 ± 0.1	OCl-8,BH 253,ESO 521SC3

Table notes. Columns 2 and 3: Central coordinates measured by us on XDSS images. Column 4: angular diameter estimated on XDSS images. Columns 5–8: Optimized central coordinates (from 2MASS data). Column 10: reddening in the object's central region (Section 4.6). Column 12: $d_{\rm GC}$ calculated using the distance of the Sun to the Galactic centre $R_o = 7.2$ kpc (Bica et al. 2006).

Tr 23 and Tr 26 are used to compare cluster parameters obtained by means of different decontamination approaches and observational data sets, and to further probe their properties. Cluster parameters for NGC 5715, Ly 4, Ly 9 and Cz 37 are derived for the first time.

To be considered as a high-probability star cluster, a candidate must present both an FS-decontaminated CMD morphology and a CM-filtered stellar RDP consistent with those of typical OCs. A third criterion would be a cluster-like MF. However, since MFs change with cluster age and are environment-dependent (Bonatto & Bica 2006, and references therein), they do not provide enough constraints to confirm or rule out OC-candidates.

The density of stars in the direction of the present objects is unprecedented as compared to our previous efforts to explore OCs in general. This work is expected to contribute not only with parameters of unstudied star clusters, but also with quantitative tools that are useful to the study of OCs projected in dense fields.

This paper is organized as follows. Section 2 contains basic properties and reviews literature data (when available) on the objects. Section 3 discusses 2MASS data and photometric uncertainties. In Section 4, we describe the FS-decontamination algorithm to be applied to CMDs, discuss its results and limitations, and derive fundamental cluster parameters. Section 5 presents definitions of the CM filters for each cluster, stellar RDPs and radial mass density profiles (MDPs), and models of the effect of varying background levels on cluster radii determination. In Section 6, MFs and cluster mass are inferred. In Section 7 aspects related to the structure and dynamical state of the present objects are discussed. Concluding remarks are given in Section 8.

2 THE TARGET OPEN CLUSTERS AND CANDIDATES

According to the OC catalogues WEBDA[2] and DAML02[3] NGC 5715, Ly 9 and Cz 37 do not have published fundamental photometric parameters. No structural parameters are available either.

van den Bergh & Hagen (1975) measured an angular diameter $D = 10$ arcmin and estimated a medium richness for NGC 5715. Ruprecht (1966) classified it as Trumpler type II 2 m, while Lyngå (1982) as III 2 m.

Ly 4 was photoelectrically studied by Moffat & Vogt (1975), but the few observed stars did not allow determination of a cluster sequence in the CMD. Its Trumpler type is IV 2 p according to Ruprecht (1966) or II 2 m (Lyngå 1982).

Carraro, Janes & Eastman (2005) photometrically studied Ly 9, however, without applying a quantitative FS decontamination. They concluded that Ly 9 is an enhancement of the dense stellar field. van den Bergh & Hagen (1975) estimated an angular diameter of $D = 6$ arcmin and medium richness. Its Trumpler type is III 1 m (Ruprecht 1966; Lyngå 1982).

Carraro et al. (2005) concluded that Cz 37 might be a real cluster superimposed on the Galactic bulge population. van den Bergh & Hagen (1975) estimated $D = 3$ arcmin and medium richness. Its Trumpler type is III 2 p (Ruprecht 1966) or II 1 m (Lyngå 1982).

Carraro et al. (2006) found that Tr 23 is an intermediate-age OC within the solar circle that deserves further attention. They applied in the analysis the FS-decontamination method by Bertelli et al. (2003), from which they obtained $E(B-V) = 0.83$, $D_{\odot} = 2.2$ kpc and age 1 Gyr. van den Bergh & Hagen (1975) derived $D = 6$ arcmin and medium richness. Its Trumpler type is II 2 p (Ruprecht 1966) or III 1 m (Lyngå 1982).

Kharchenko et al. (2005) employed the ASCC-2.5 catalogue with limiting magnitude $V \approx 14$ to derive parameters for 520 OCs, using proper motion and photometric criteria to separate probable members from FSs. However, owing to distance and reddening limitations, the fainter cluster parameters rely on a few stars. For Tr 26 they derived $E(B-V) = 0.14$, $D_{\odot} = 2.8$ kpc, age 240 Myr, and core and cluster radii of 4.2 and 9.6 arcmin, respectively. van den Bergh & Hagen (1975) derived $D = 6$ arcmin and medium richness. Its Trumpler type is II 2 p (Ruprecht 1966) or III 1 m (Lyngå 1982).

In Fig. 1, we show optical XDSS[4] images of Tr 26 (left-hand panel, *B* band) and Cz 37 (right-hand panel, *R* band). Tr 26 presents a lower contrast with respect to the background than Cz 37. XDSS *R* images of Ly 4 (left-hand panel) and Ly 9 (right-hand panel) are shown in Fig. 2, while in Fig. 3 we present XDSS *R* images of Tr 23 (left-hand panel) and NGC 5715 (right-hand panel). The field of Tr 23 presents significant differential absorption, especially in the north–south direction (Section 3.1). All objects appear to be heavily contaminated by dense stellar fields.

Table 1 provides information on the objects. Right ascension, declination and angular diameter (columns 2–4) were visually measured by us on XDSS images (Figs 1–3) as a first order approximation to the objects' centre and dimension. However, RDPs (Section 5.2) built based on the XDSS central coordinates of NGC 5715, Tr 23, Ly 4 and Ly 9 presented a dip at $R = 0$. Consequently, new coordinates were searched to maximize the central density of stars by examining histograms for the number of stars in 0.5-arcmin-wide bins of right ascension and declination on CM-filtered photometry (Section 5.1). The new central coordinates and the corresponding Galactic longitude and latitude are given in columns 5–8 of Table 1. Age, central reddening, distance from the Sun and Galactocentric distance based on 2MASS data (Section 4.6) are given in columns 9–12. Additional designations in column 13 of Table 1 are BH (van den Bergh & Hagen 1975) and ESO (Lauberts 1982); previous ones are given in Alter et al. (1970).

3 2MASS PHOTOMETRY

J, H and K_s 2MASS photometry was extracted in circular fields centred on the optimized coordinates of the objects (columns 5 and 6 of Table 1) using VIZIER.[5] Our previous experience with OC analysis (Section 1) shows that as long as no other populous cluster is present in the field, and differential absorption is not prohibitive, large extraction areas can provide the required statistics for a consistent FS characterization. Based on this, we used extraction radii (column 5 of Table 2) significantly larger than the respective limiting radii (Section 5.2 and column 7 of Table 4) of the present objects. As photometric quality constraint, 2MASS extractions were restricted to stars with magnitudes (i) brighter than those of the 99.9 per cent PSC completeness limit[6] in the cluster direction, and (ii) with errors in J, H and K_s smaller than 0.2 mag. The 99.9 per cent completeness limits are different for each cluster, varying with Galactic coordinates. They are given in columns 2–4 of Table 2, respectively, for

[2] www.univie.ac.at/webda//.

[3] www.astro.iag.usp.br/wilton/.

[4] Extracted from the Canadian Astronomy Data Centre (CADC), at http://cadcwww.dao.nrc.ca/.

[5] http://vizier.u-strasbg.fr/viz-bin/VizieR?-source=II/246.

[6] Following the Level 1 Requirement, according to http://www.ipac.caltech.edu/2mass/releases/allsky/doc/sec6_5a1.html.

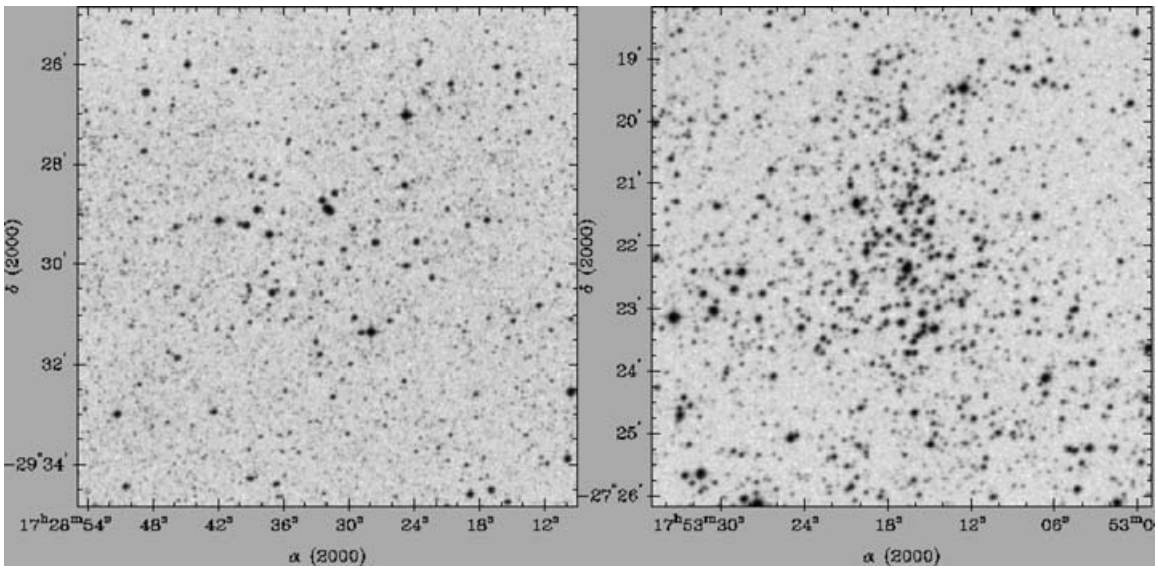

Figure 1. Left-hand panel: 5×5-arcmin^2 XDSS *B* image of Tr 26. Right-hand panel: 4×4-arcmin^2 XDSS *R* image of Cz 37. Images centred on the optimized coordinates (columns 5 and 6 of Table 1).

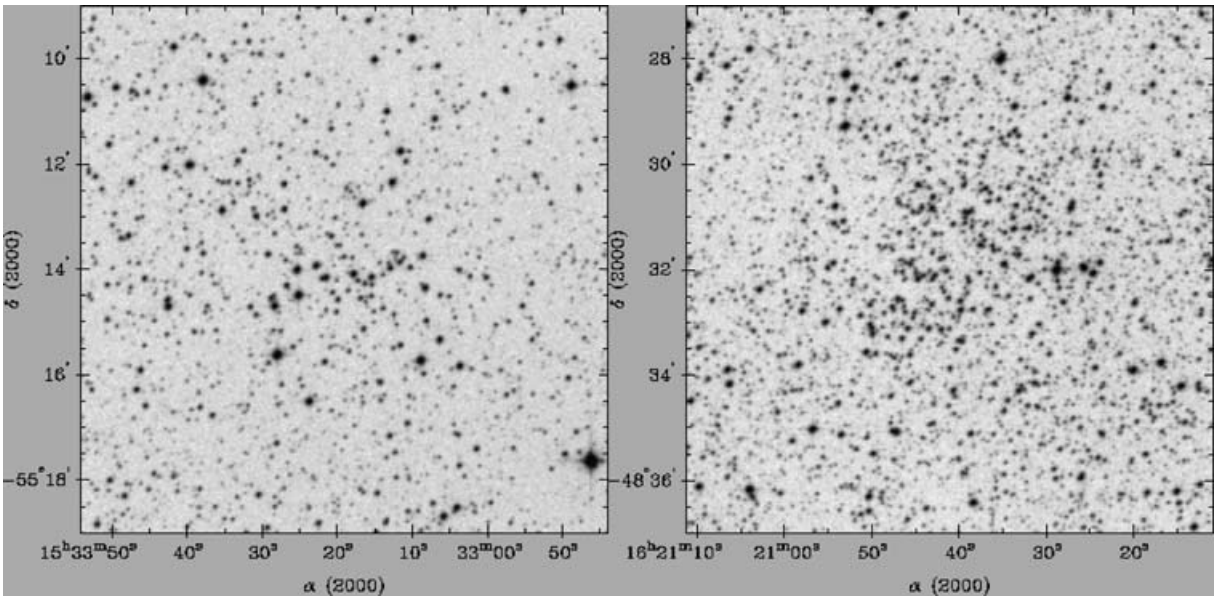

Figure 2. The same as Fig. 1 for the 5×5-arcmin^2 (XDSS *R*) field around Ly 4 (left-hand panel) and the 5×5-arcmin^2 (XDSS *R*) field around Ly 9 (right-hand panel).

J, *H* and K_s. For reddening transformations we use the relations $A_J/A_V = 0.276$, $A_H/A_V = 0.176$, $A_{K_s}/A_V = 0.118$, and $A_J = 2.76 \times E(J-H)$ (Dutra, Santiago & Bica 2002), assuming a constant total-to-selective absorption ratio $R_V = 3.1$.

To objectively characterize the distribution of 2MASS photometric uncertainties in the fields of the present objects, we show Fig. 4 cumulative histograms with the fraction of stars as a function of uncertainties for the 3 bands. Projected areas sampled in the histograms correspond to the respective limiting radius of each object (Section 5.2). The distribution of photometric uncertainties is similar among the fields sampled. More than ≈80 per cent of the stars in NGC 5715, Ly 4, Tr 23 and Cz 37 have *J* and *H* uncertainties smaller than 0.06 mag; for K_s this fraction is slightly smaller. In Tr 26 and Ly 9, the 0.06 mag fractions are ≈70 per cent. 2MASS uncertainties are in general larger than those of CCD photometry. However, for most stars in the present objects they are still small enough to provide reliable values of magnitude and colours. Besides, for this kind of study large surrounding fields are necessary for statistical representativity of FSs (Section 4) and long-base RDPs (Section 5.2), which in general are not available in the optical.

In Fig. 5, we present the analysis of NGC 5715, by means of $J \times (J-H)$ and $J \times (J-K_s)$ CMDs extracted from a central ($R = 3$ arcmin) region. The extension of this extraction corresponds to about twice the core radius and somewhat larger than half the limiting radius (Section 5). This extraction provides an adequate contrast (in terms of density of stars) between CMD sequences of the object

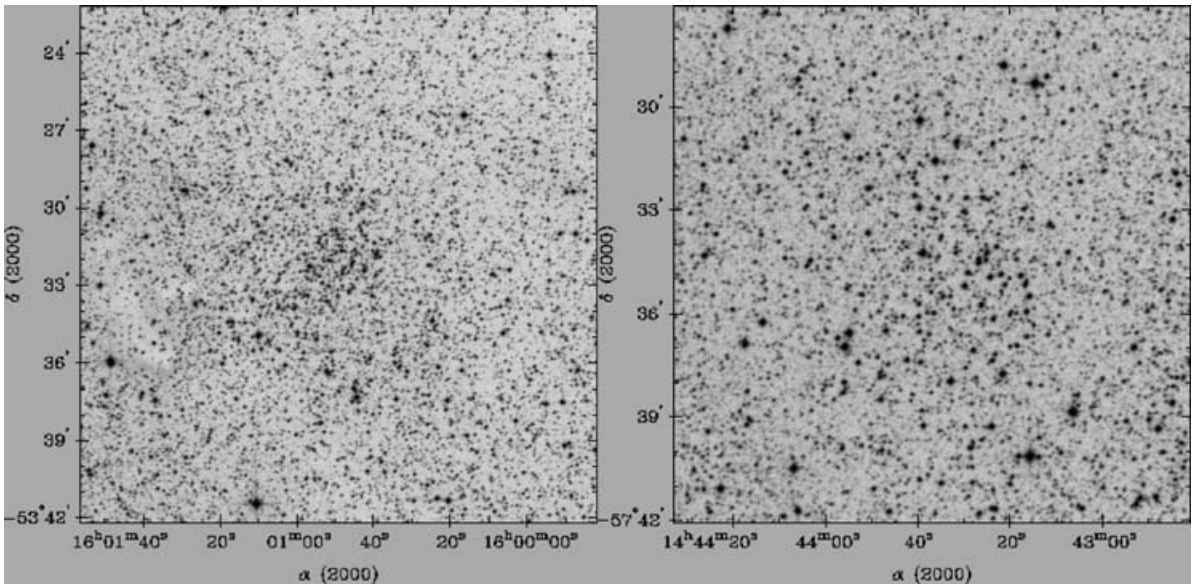

Figure 3. The same as Fig. 1 for the 10×10 arcmin^2 (XDSS *R*) field around Tr 23 (left-hand panel) and the 7.5×7.5 arcmin^2 (XDSS *R*) field around NGC 5715 (right-hand panel).

Table 2. Details on 2MASS photometry.

Cluster	Completeness limit J (mag)	H (mag)	K_s (mag)	$R_{\rm ext}$ (arcmin)	Comparison field (arcmin)
(1)	(2)	(3)	(4)	(5)	(6)
NGC 5715	15.8	15.1	14.3	30	10–30
Lyngå 4	15.5	15.1	14.3	50	20–50
Trumpler 23	15.5	15.0	14.2	40	[a]
Lyngå 9	15.5	14.8	14.0	30	10–30
Trumpler 26	14.2	13.5	12.5	50	20–50
Czernik 37	15.0	14.0	13.2	40	10–40

Table notes. Column 5: 2MASS extraction radius.
[a]Because of heavy differential absorption, the comparison field of Tr 23 was taken from two $R = 5$ arcmin circular regions located at 20′ east and west of the cluster centre (Section 3.1).

and offset field. Photometry was limited in magnitude according to columns 2–4 of Table 2; the error bars show that photometric uncertainties, although increasing for faint stars (Fig. 4), are not large to the point of producing smeared CMDs. Bulge stars are conspicuous in the field of NGC 5715, as shown in both CMDs (top panels), especially for $(J - H) \gtrsim 0.75$ and $(J - K_{\rm s}) \gtrsim 1.0$. However, comparison of the central CMDs (top panels) with those of the equal area offset field (middle panels) suggests an excess of stars for bluer colours, which is indicative of an MS. Evidence of a giant clump is also present in both CMDs. The statistical significance of this excess is further detached on the FS-decontaminated CMD morphology (bottom panels of Fig. 5). We explore FS-decontaminated CMD morphology further in Section 4.

Similar analyses involving $J \times (J - H)$ and $J \times (J - K_{\rm s})$ CMDs were applied to the remaining objects. In all cases we show CMDs of extractions taken from regions with radius intermediate between core and limiting radii. For the sake of simplicity only the $J \times (J - H)$ CMDs are shown in Figs 6 and 7. In all cases, varying proportions of bulge stars can be seen in the observed CMDs (top panels). Disentangling cluster and field sequences in such dense fields requires a quantitative method (Section 4).

3.1 Spatially variable absorption in the field of Tr 23

Some peculiarities associated with variable absorption that affects star sequences in the CMD of Tr 23 are important to be discussed.

Fig. 3 indicates the presence of important variable absorption in the optical field of Tr 23. To investigate its spatial distribution we plot in the top panels of Fig. 8 the 2MASS position of each star (with respect to the central coordinates – Table 1) both in the observed (left-hand panel) and in the CM-filtered (Section 5.1) photometry (right-hand panel). The distribution of stars in both panels is affected by differential absorption, especially in the north–south direction.

This trend is confirmed by the linear profiles (number of stars per bin) extracted along declination (bottom left-hand panel) and right-ascension (bottom right-hand panel) directions, centred on the coordinates of Tr 23 (Table 1). The field along the east–west direction is more uniform than the north–south one. To minimize differential absorption effects, we take as comparison field the average of two circular regions of 5 arcmin in radius shifted 20 arcmin east and west off the centre of Tr 23. CMDs of a central ($R = 3$ arcmin) and offset field regions, as well as the FS-decontaminated one of Tr 23 are shown in Fig. 6 (left-hand panels).

4 FIELD-STAR DECONTAMINATION IN COLOUR–MAGNITUDE DIAGRAMS AND CLUSTER FUNDAMENTAL PARAMETERS

Important FS contamination is conspicuous in the observed CMDs of the present, low-latitude objects, projected against bulge directions (upper panels of Figs 5–7). Quantitative FS decontamination becomes fundamental to determine the nature of these objects, as real star clusters or random fluctuations of the dense background stellar density, that is, asterisms.

Disentangling cluster and FSs is an important – but difficult – task, especially if dense fields and poorly populated clusters are involved. Ideally, cluster member identification is more constrained when photometric and proper motion data are available for a large number of individual stars (e.g. Dias et al. 2006). However, for most star clusters, distant ones in particular, proper motion data are

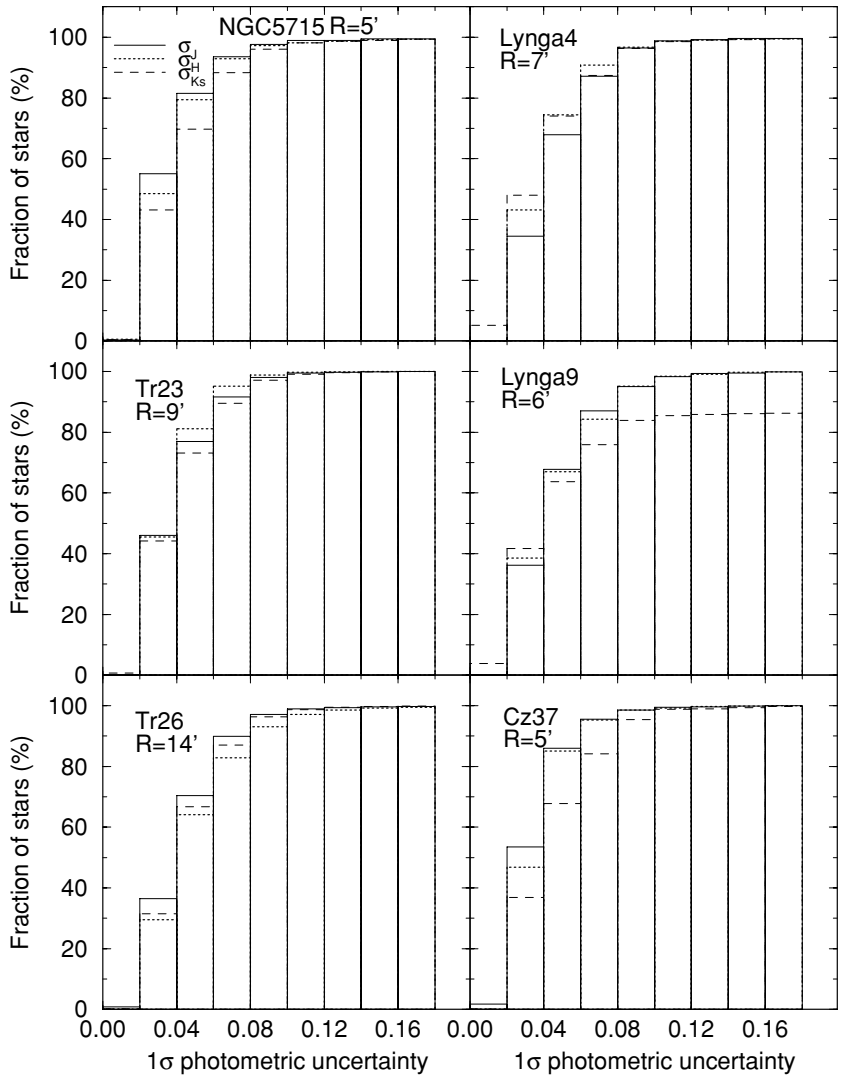

Figure 4. Quantitative evaluation of 2MASS photometric errors by means of cumulative histograms with the number of stars as a function of uncertainties. In all cases, most of the stars have uncertainties smaller than 0.06 mag.

not available. Thus the task has to be done using only photometry, by means of statistical comparison of star samples taken from the cluster region and offset field.

4.1 Description of the FS-decontamination algorithm

To uncover the intrinsic CMD morphology we use an upgraded version of the FS-decontamination algorithm previously applied in the analysis of low-contrast (Bica & Bonatto 2005), embedded (Bonatto et al. 2006), young (Bonatto et al. 2006b), and faint (Bica et al. 2006) OCs. Sampling small CMD regions, the algorithm works on a statistical basis that takes into account the relative number-densities of stars in a cluster region and comparison field. It can be applied to the full cluster region ($0 \leqslant R \leqslant R_{\rm lim}$) or inner regions such as core and/or halo. This upgraded version of the algorithm works with three dimensions, the J magnitude and the $(J-H)$ and $(J-K_{\rm s})$ colours, considering as well the respective 1σ uncertainties in the 2MASS bands, σ_J, σ_H and $\sigma_{K_{\rm s}}$. These are the 2MASS colours that provide the maximum variance among cluster CMD sequences for OCs of different ages (e.g. Bonatto, Bica & Girardi 2004).

Basically, the algorithm (i) divides the full range of magnitude and colours of a given CMD into a 3D grid whose cubic cells have axes along the J, $(J-H)$ and $(J-K_{\rm s})$ directions, (ii) computes the expected number-density of FSs in each cell based on the number of comparison FSs with magnitude and colours compatible with those of the cell, and (iii) randomly subtracts the expected number of FSs from each cell. Consequently, this method is sensitive to local variations in FS contamination with magnitude and colours. To simplify notation we use the definitions $\chi = J$, $\xi = (J-H)$ and $\zeta = (J-K_{\rm s})$.

Cell dimensions are $\Delta\chi = 0.5$ and $\Delta\xi = \Delta\zeta = 0.2$, except in Cz 37 where $\Delta\xi = \Delta\zeta = 0.15$. These values are large enough to allow sufficient star-count statistics in individual cells and small enough to preserve the morphology of different CMD evolutionary sequences. Besides, 2MASS photometric uncertainties for most stars of the present objects are considerably smaller than the adopted cell dimensions (Section 3 and Fig. 4).

To illustrate the process, consider a CMD cell whose sides in the (χ, ξ, ζ) space have coordinates $(\chi_{\rm c} \pm \Delta\chi/2, \xi_{\rm c} \pm \Delta\xi/2, \zeta_{\rm c} \pm \Delta\zeta/2)$, where $(\chi_{\rm c}, \xi_{\rm c}, \zeta_{\rm c})$ are the cell's central coordinates. We

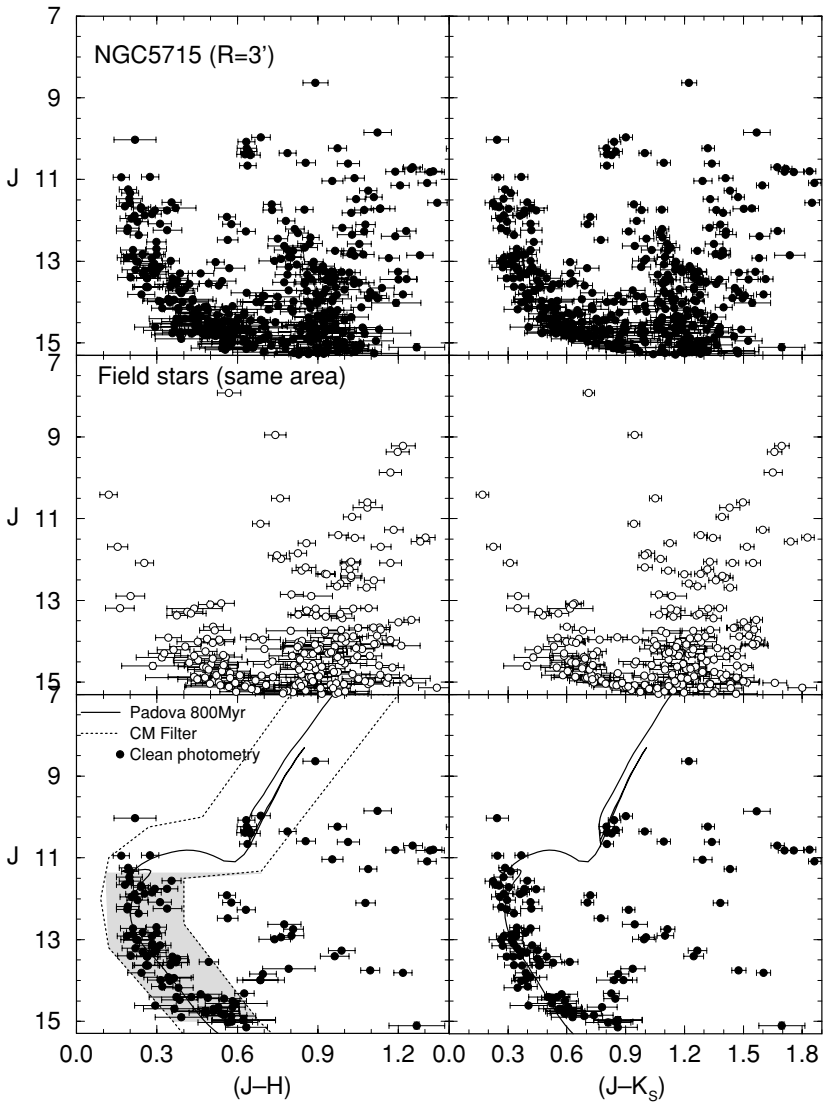

Figure 5. Top-left panel: observed $J \times (J - H)$ CMD of a central ($R = 3$ arcmin) region of NGC 5715, which shows some contamination of bulge stars, especially for $(J - H) \gtrsim 0.75$. Middle-left panel: FSs taken from the comparison field with a projected area equal to that in the above panel. Bottom-left panel: FS decontaminated CMD together with the fit of the 800 Myr Padova isochrone (solid line) and the CM filter (Section 5.1) used to isolate cluster MS/evolved stars (dotted line). Completeness limit for this cluster ($J = 15.8$) is just below the bottom of the CMDs. The magnitude range for MF purposes is shown as a shaded region about the MS. Right panels: the same for the $J \times (J - K_s)$ CMD. The giant clump and a significant fraction of the MS are conspicuous in both colours.

use Gaussian distributions of magnitude[7] and colours to compute the probability of a star with CMD coordinates $(\bar{\chi} \pm \sigma_\chi, \bar{\xi} \pm \sigma_\xi, \bar{\zeta} \pm \sigma_\zeta)$ to be found within that cell. In this way, computations take into account magnitude and colour uncertainties, in the sense that stars with large uncertainties may have a non-negligible probability of populating more than one CMD cell. We assume that probable cluster stars are distributed in the region $0 < R < R_{\rm lim}$, with projected area $A_{\rm cl}$, while FSs are taken from the offset field region ($R > R_{\rm lim}$), with projected area $A_{\rm fs}$. The expected FS number-density ($\rho_{\rm fs}^{\rm cell}$) in a given cell is computed by summing up the individual probability ($P_{\rm fs}^{\rm cell}$) of all offset FSs ($N_{\rm fs}$) to be found in the cell, divided by the offset field area, $\rho_{\rm fs}^{\rm cell} = P_{\rm fs}^{\rm cell}/A_{\rm fs}$, where

$$P_{\rm fs}^{\rm cell} = \sum_{i=1}^{N_{\rm fs}} \int\int\int P_i(\chi, \bar{\chi}_i; \xi, \bar{\xi}_i; \zeta, \bar{\zeta}_i)\, {\rm d}\chi\, {\rm d}\xi\, {\rm d}\zeta.$$

$P_i(\chi, \bar{\chi}_i; \xi, \bar{\xi}_i; \zeta, \bar{\zeta}_i)$ represents the probability of the ith offset FS, with CMD coordinates $(\bar{\chi}_i, \bar{\xi}_i, \bar{\zeta}_i)$ and uncertainties $(\sigma_{\chi_i}, \sigma_{\xi_i}, \sigma_{\zeta_i})$, to have the magnitude and colours (χ, ξ, ζ). Integrals are carried over the cell's extension in each dimension, $\chi_{\rm c} - \Delta\chi/2 \leqslant \chi \leqslant \chi_{\rm c} + \Delta\chi/2$, $\xi_{\rm c} - \Delta\xi/2 \leqslant \xi \leqslant \xi_{\rm c} + \Delta\xi/2$ and $\zeta_{\rm c} - \Delta\zeta/2 \leqslant \zeta \leqslant \zeta_{\rm c} + \Delta\zeta/2$, respectively; they basically reduce to error functions computed at the cell borders.

We do the same to compute the number-density of observed (cluster + FS) stars in the cell, $\rho_{\rm obs}^{\rm cell} = P_{\rm obs}^{\rm cell}/A_{\rm cl}$. In this case we consider only stars that are in the cluster region ($0 \leqslant R \leqslant R_{\rm lim}$). Thus, the

[7] For example, $P(J, \bar{J}) = \frac{1}{\sqrt{2\pi}\sigma_J}\, {\rm e}^{(-1/2)[(J-\bar{J})/\sigma_J]^2}$.

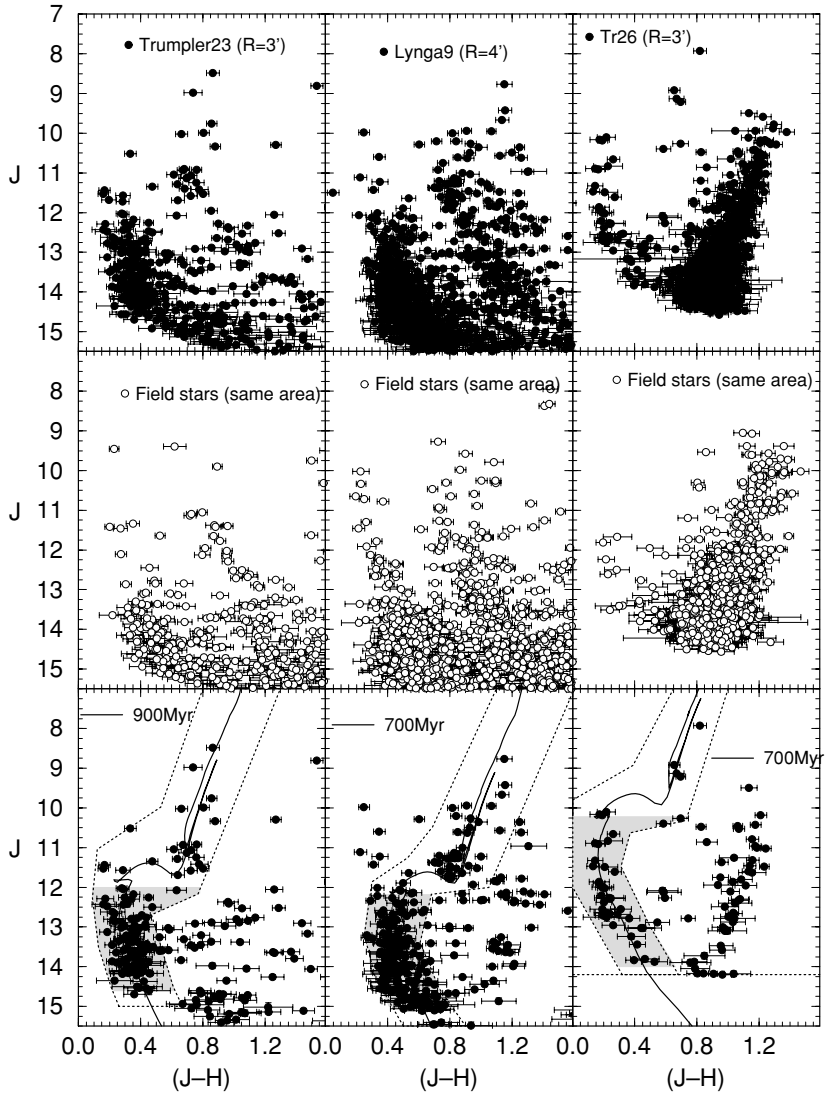

Figure 6. Same as Fig. 5 for the $J \times (J-H)$ CMDs of Tr 23 (left panels), Ly 9 (middle panels), and Tr 26 (right panels). Completeness limits are $J = 15.5$ for Tr 23 and Ly 9, and $J = 14.2$ for Tr 26. Isochrone ages are 900 Myr (Tr 23) and 700 Myr (Tr 26 and Ly 9).

expected number of FSs in the cell is given by $n_{\rm fs}^{\rm cell} = \frac{\rho_{\rm fs}^{\rm cell}}{\rho_{\rm obs}^{\rm cell}} \times n_{\rm obs}^{\rm cell}$, where $n_{\rm obs}^{\rm cell}$ is the number of observed stars (at $R \leqslant R_{\rm lim}$) located in the cell. The number of probable member stars in the cell is $n_{\rm cl}^{\rm cell} = n_{\rm obs}^{\rm cell} - n_{\rm fs}^{\rm cell}$. Finally, the total number of probable cluster members is obtained by summing $n_{\rm cl}^{\rm cell}$ over all CMD cells, $N_{\rm cl} = \sum_{\rm cell} n_{\rm cl}^{\rm cell}$.

As a last step, to minimize potential artificialities introduced by the choice of parameters, we apply the decontamination algorithm for three different grid specifications in each dimension. For instance, for a CMD grid beginning at magnitude J_0 (and cell width ΔJ), we also include additional runs for $J_0 \pm \frac{1}{3}\Delta J$. Considering as well similar variations for the two colours, 27 different outputs are obtained, from which we compute the average number of probable cluster stars $\langle N_{\rm cl}\rangle$. Typical standard deviations of $\langle N_{\rm cl}\rangle$ are at the $\approx$2.5 per cent level. The final FS-decontaminated CMD contains the $\langle N_{\rm cl}\rangle$ stars with the highest number-frequencies.

4.2 FS subtraction efficiency

Working with densities inevitably results in fractional numbers of FSs in some cells. Fractions, in those cases, are rounded off to the nearest integer, however, limited to the number of observed stars present in the cell ($n_{\rm fs}^{\rm cell} \leqslant n_{\rm obs}^{\rm cell}$). To take this effect into account, we compute for each cell the difference between the expected number of FSs and the actual number of subtracted stars. Summing this difference over all cells gives us an estimate of the total number of unsubtracted FSs ($\tilde{N}_{\rm fs}$), as well as a measure of the global subtraction efficiency ($f_{\rm sub}$) of the process. The unsubtracted stars cannot be deleted from CMDs, since $\tilde{N}_{\rm fs}$ results from the sum of star fractions over all cells. However, $f_{\rm sub}$ can be used to compute the corrected fraction of cluster member stars. Subtraction efficiency and corrected fraction of cluster members for the present objects are given in Table 3.

Small values of ΔJ, $\Delta(J-H)$ and $\Delta(J-K_{\rm s})$ increase the frequency of cells with fractional values of FSs, which in turn produce small subtraction efficiencies. Large values, on the other hand, increase subtraction efficiencies, but tend to degrade CMD resolution, which may be necessary to disentangle cluster and FS sequences. The adopted values of cell dimensions (see above) are a compromise between subtraction efficiency and CMD resolution at the 2MASS photometric uncertainties.

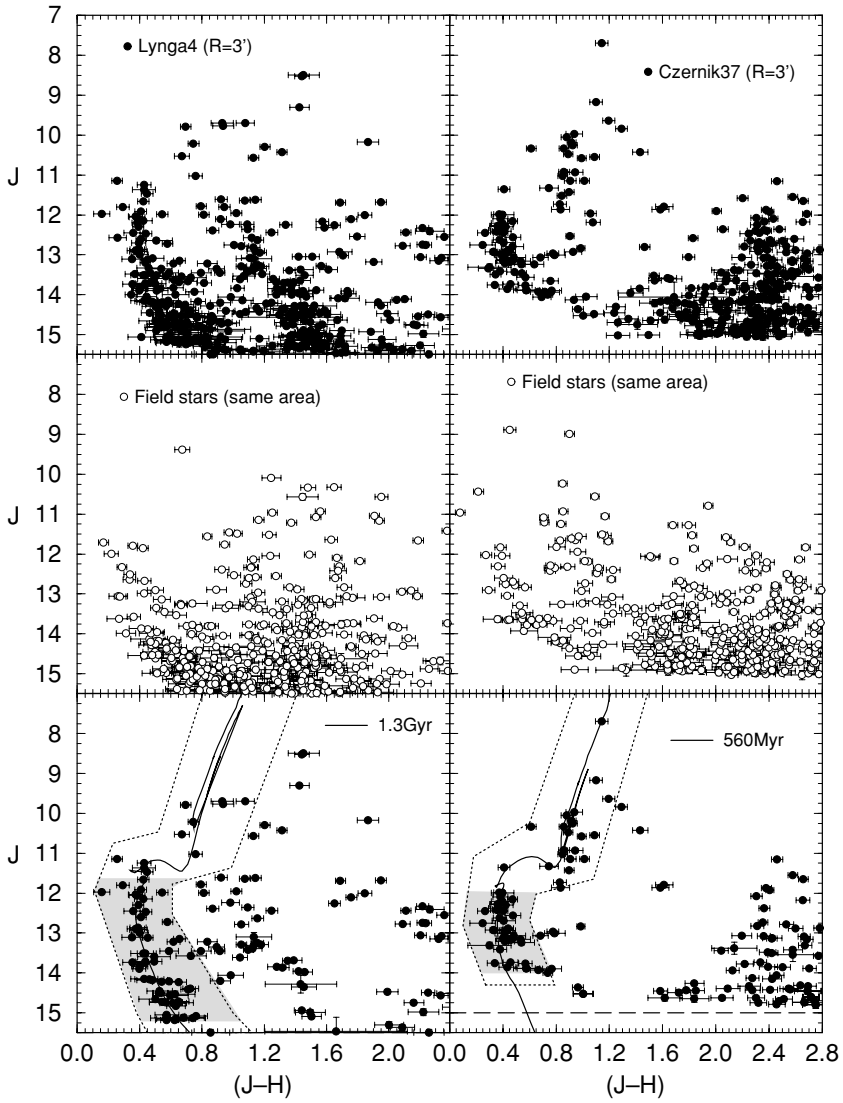

Figure 7. Same as Fig. 5 for the $J \times (J - H)$ CMDs of Ly 4 (left panels) and Cz 37 (right panels). Completeness limits are $J = 15.5$ for Ly 4 and $J = 15.0$ for Cz 37. Isochrone ages are 1.3 Gyr (Ly 4) and 560 Myr (Cz 37).

In principle, inclusion of additional dimensions such as the H or K_s magnitudes, could produce more constrained results. On the other hand, this would as well reduce the number of stars in the multi-dimensional cells and, consequently, the subtraction efficiency would become significantly reduced.

4.3 Application to the objects and results

The output of the FS-decontamination algorithm can be examined from two different, but complementary, perspectives, that is, (i) the dependence of FS contamination (or alternatively, fraction of probable cluster stars) on apparent magnitude, and (ii) distance to the cluster centre.

Fig. 9 provides histograms that show for each object the fraction of stars before and after FS decontamination as a function of J magnitude, sampled in bins of $\Delta J = 1$ mag. In all cases, the area sampled by the histograms ranges from the centre to the limiting radius (Section 5). As expected from their almost central directions, FS contamination in the fields of the present six objects dominates the observed photometry ($\gtrsim$90 per cent – Table 3), increasing exponentially for faint magnitudes. Fig. 9 shows that in all cases the increase with magnitude of the residual FS contribution (subtraction of the probable cluster stars from the observed ones) is well represented by the exponential growth curve $f_{\rm FS}(J) \propto e^{(J/\epsilon_J)}$, with a magnitude-scale factor $\epsilon_J \approx 1.2 \pm 0.1$. Consequently, at the 2MASS completeness limits (Section 3), FSs should represent more than ≈90 per cent of the stars populating CMDs of bulge-projected OCs. The above discussion further stresses the difficulties associated with the study of OCs projected against central parts of the Galaxy, especially to access the low MS of poorly populated objects.

With respect to radial distribution, Table 3 provides statistics on the fraction of probable cluster members (considering the full magnitude range), both for the observed and for the CM-filtered photometries, for annular extractions located at different distances from the central positions. Probable cluster member fractions have been corrected for the respective subtraction efficiencies. In all cases, FSs dominate over cluster members in the observed photometry (top half of Table 3), since the former contribute with more than ≈90 per cent to the stars in the overall ($R \leqslant R_{\rm lim}$) CMDs of the present objects. However, as expected from star clusters, the fraction of probable

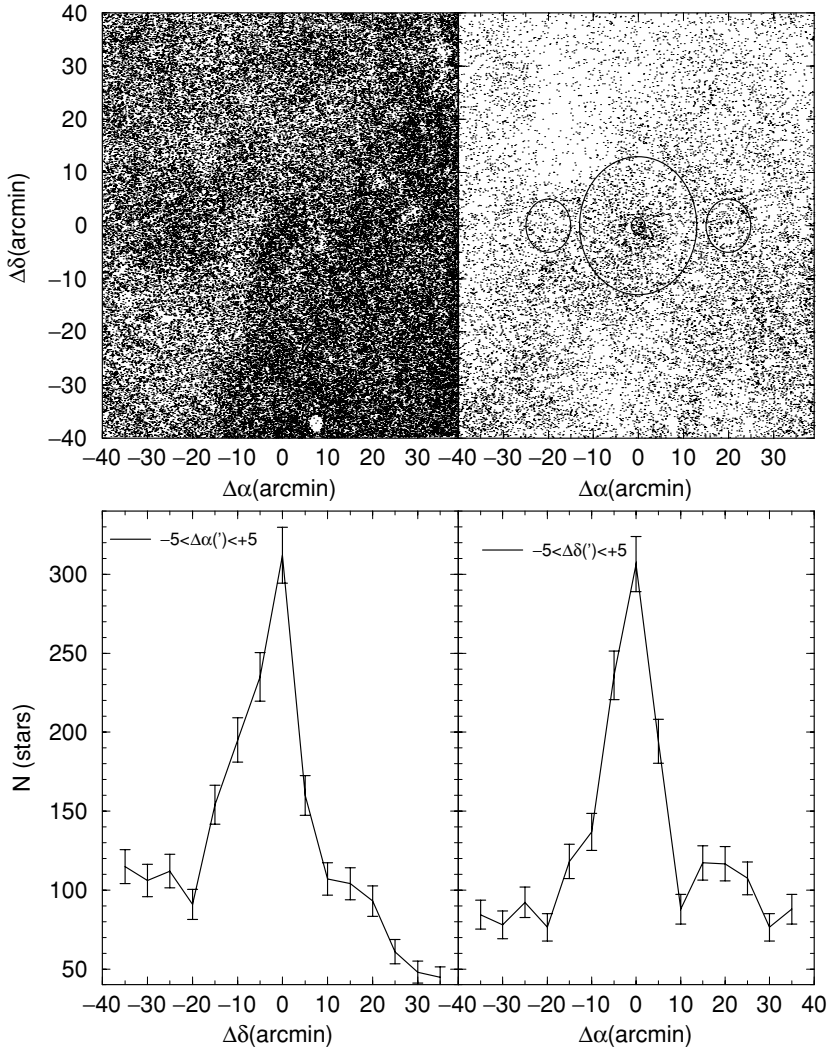

Figure 8. Top-left panel: projected position of the stars in the field of Tr 23. Top-right: same as before for the CM-filtered photometry; core and limiting radii, as well as the east–west comparison fields are marked off. Bottom-left: north–south profile extracted within the central stripe located at $-5 \leqslant \alpha(\mathrm{arcmin}) \leqslant +5$. Bottom-right: east-west profile extracted within the stripe $-5 \leqslant \delta(\mathrm{arcmin}) \leqslant +5$.

members systematically increases for smaller radii, reaching a maximum at the centre. In the present objects, central cluster member fractions (observed photometry) range from ≈11 per cent (Tr 26) to ≈46 per cent (Cz 37).

The above features are enhanced in the output of the FS decontamination when applied to CM-filtered data (bottom half of Table 3). As suggested by previous works (e.g. Bonatto & Bica 2005; Bonatto et al. 2006b), CM filters allow detection of cluster structures at larger distances from the cluster centre than with observed photometry. The elimination of most of the obvious non-cluster stars provided by the CM filter makes the FS contamination drop to ∼55–87 per cent for the present objects. This, in turn, allows a better determination of cluster structural parameters and dimension. Indeed, central cluster member fractions become significantly larger, as compared to those obtained with observed photometry, ranging from ≈45 per cent (Ly 4) to ≈79 per cent (Tr 26).

Stars that remain in the CMD after application of the FS decontamination are in cells where the stellar density presents a clear excess over the field. Consequently, they have a significant probability of being cluster members. In crowded field regions, however, FS density at faint magnitudes (which presents an exponential growth with magnitude – Fig. 9) may be equal or even larger than that measured for the cluster. In such cases the present FS-decontamination algorithm naturally truncates the MS at about the same level as that set by the 2MASS completeness limits (Table 2).

4.4 Field-star decontaminated CMDs

FS-decontaminated CMDs of the present objects are shown in the bottom panels of Figs 5–7, where we also include the respective CM filters (Section 5.1). As expected, most of the red and faint stars were indicated as background by the decontamination algorithm. In all cases, the remaining stars in the CMDs populate up sequences of typical intermediate-age OCs, with marked TO and GB. NGC 5715 is a clear cluster with a populated MS spanning ≈3 mag and a conspicuous clump. Tr 23 is a cluster (as concluded also by Carraro et al. 2006) as denoted by the populated MS and a conspicuous clump, although residual FS contamination is more important than in NGC 5715. Ly 9 exhibits prominent MS and clump indicative of a cluster (Section 5.4). Tr 26 is a cluster with a rather populated

Table 3. Spatial properties of the FS decontamination.

	Observed photometry																	
	NGC 5715			Ly 4			Tr 23			Ly 9			Tr 26			Cz 37		
ΔR (arcmin) (1)	N (*) (2)	f_{sub} (per cent) (3)	f_{cl} (per cent) (4)	N (*) (5)	f_{sub} (per cent) (6)	f_{cl} (per cent) (7)	N (*) (8)	f_{sub} (per cent) (9)	f_{cl} (per cent) (10)	N (*) (11)	f_{sub} (per cent) (12)	f_{cl} (per cent) (13)	N (*) (14)	f_{sub} (per cent) (15)	f_{cl} (per cent) (16)	N (*) (17)	f_{sub} (per cent) (18)	f_{cl} (per cent) (19)
0–2	193	84 ± 3	26.8 ± 5.8	218	91 ± 1	28.6 ± 5.1	211	81 ± 2	42.4 ± 4.6	311	80 ± 2	35.7 ± 4.0	329	91 ± 2	10.8 ± 5.5	204	72 ± 4	46.3 ± 5.6
2–4	486	91 ± 1	9.0 ± 4.2	542	90 ± 1	9.3 ± 4.0	564	90 ± 2	28.5 ± 3.5	722	86 ± 1	10.0 ± 3.5	1028	96 ± 1	13.0 ± 2.9	495	71 ± 3	12.2 ± 7.2
4–6	736	89 ± 1	0.0 ± 3.8	892	90 ± 1	6.9 ± 3.1	843	86 ± 1	18.1 ± 3.3	1063	85 ± 1	0.0 ± 3.3	1656	95 ± 1	8.4 ± 2.8	851	67 ± 2	8.4 ± 6.4
6–8	–		–	1274	91 ± 1	7.8 ± 2.6	1016	82 ± 1	2.8 ± 3.3	–		–	2192	87 ± 1	2.8 ± 2.9	1203	69 ± 1	0.2 ± 7.4
8–10	–		–	1546	90 ± 1	1.6 ± 2.5	1256	84 ± 1	0.0 ± 3.0	–		–	2822	92 ± 1	1.9 ± 2.2	–		–
10–12	–		–	–		–	–		–	–		–	3443	91 ± 1	2.5 ± 2.1	–		–
12–14	–		–	–		–	–		–	–		–	4071	92 ± 1	2.0 ± 1.9	–		–
Total	995	90 ± 1	6.8 ± 3.2	2241	91 ± 1	7.4 ± 2.0	3237	85 ± 1	9.2 ± 1.8	2096	86 ± 1	7.4 ± 2.2	15541	92 ± 1	6.3 ± 1.5	1149	65 ± 1	7.1 ± 6.9
	CM-filtered photometry																	
0–2	84	95 ± 4	56.3 ± 5.4	95	95 ± 3	44.9 ± 6.0	105	94 ± 4	63.0 ± 4.4	187	92 ± 4	58.6 ± 3.6	36	84 ± 11	79.0 ± 5.2	50	74 ± 11	78.7 ± 5.7
2–4	175	95 ± 1	33.9 ± 5.1	196	94 ± 1	16.9 ± 6.0	215	98 ± 1	45.6 ± 4.0	309	97 ± 1	23.0 ± 4.6	45	99 ± 5	42.4 ± 10.5	55	89 ± 6	36.5 ± 9.7
4–6	271	90 ± 1	1.0 ± 7.5	300	94 ± 1	5.1 ± 5.6	316	98 ± 1	37.0 ± 3.8	426	95 ± 1	6.1 ± 4.7	60	90 ± 3	24.2 ± 5.5	85	92 ± 4	31.4 ± 8.6
6–8	–		–	445	96 ± 1	11.9 ± 4.3	329	95 ± 2	16.6 ± 5.4	620	97 ± 1	10.5 ± 3.8	85	99 ± 2	26.6 ± 8.2	101	81 ± 3	4.8 ± 10.4
8–10	–		–	512	92 ± 1	1.4 ± 4.4	375	93 ± 1	6.4 ± 5.0	–		–	79	88 ± 2	0.0 ± 12.6	–		–
10–12	–		–	–		–	–		–	–		–	120	98 ± 2	17.7 ± 8.0	–		–
12–14	–		–	–		–	–		–	–		–	111	92 ± 2	0.0 ± 5.4	–	–	
TF	348	96 ± 2	30.8 ± 4.0	809	97 ± 1	14.8 ± 3.8	1140	97 ± 1	28.0 ± 2.3	922	97 ± 1	21.9 ± 2.7	536	98 ± 1	13.1 ± 4.2	158	92 ± 3	45.2 ± 5.8

Table notes. Columns 2, 5, 8, 11, 14, and 17: number of stars in the region specified in Column 1. Columns 3, 6, 9, 12, 15, and 18: subtraction efficiency; Columns 4, 7, 10, 13, 16 and 19: corrected fraction of probable member stars. Total fields (TF) correspond to extractions with radii $R = 5.0'$ (NGC 5715), $R = 7'$ (Ly 4), $R = 9'$ (Tr 23), $R = 6.1'$ (Ly 9), $R = 14'$ (Tr 26), and $R = 5.2'$ (Cz 37).

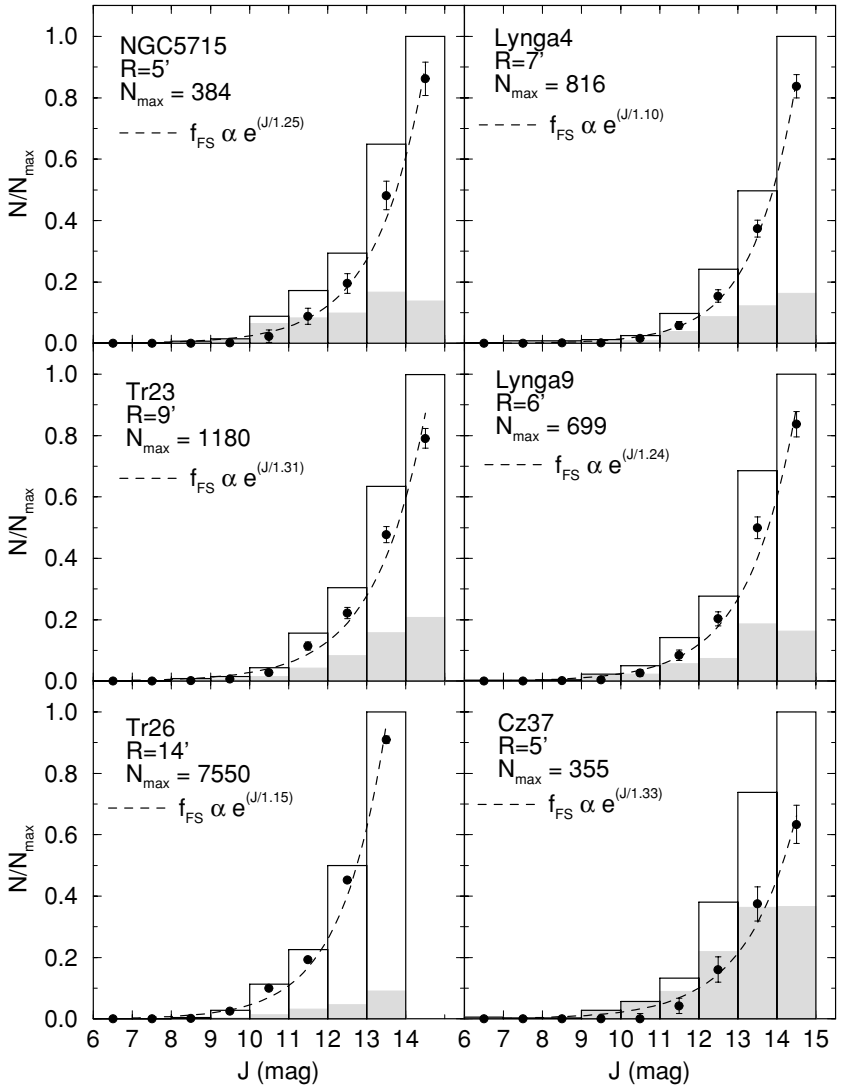

Figure 9. Fraction of stars before (empty histogram) and after (gray) FS decontamination as a function of magnitude. Regions sampled by the histograms correspond to the limiting radius of each cluster. For clarity, histograms were normalized to the number of stars in the highest bin. The residual FS contribution (filled circles) is well represented by an exponential growth curve $f_{\rm FS}({\rm J}) \propto e^{(J/\epsilon_J)}$ (dashed line).

MS considerably bluer than the bulge star contamination. Ly 4 is a more complex object whose FS-decontaminated CMD suggests an MS but residual contamination is important throughout the CMD. However, RDPs strongly indicates a cluster nature (Section 5.2 and Fig. 10). Cz 37 presents sequences considerably bluer than the field which favours the analysis. It displays about 2 mag of the MS and an apparently contaminated clump. However, RDPs of MS and giant clump taken separately (Section 5.5 and Fig. 10) show that we are dealing with a cluster.

Residual bulge star contamination occurs in the CMDs of the 2 most centrally located objects, Tr 26 (bottom panel of Fig. 6) and Cz 37 (Fig. 7). However, the fractions of non-subtracted bulge stars with respect to the observed ones are ≈7 per cent and ≈26 per cent for $R \leqslant 3$ arcmin, respectively, consistent with the subtraction efficiencies (Table 3).

As described above (Section 4.1), the FS-decontamination algorithm considers only magnitude and colour properties of stars to compute the expected number of FSs in CMD cells. As a consequence, stars in a given CMD cell (that can have any radial coordinate) have the same probability of being deleted. However, star clusters have stellar densities higher at the core than the halo. Thus, in the case of real star clusters, random subtraction of stars in cells tends to artificially change the intrinsic statistics of the radial distribution of stars. In other words, FS-decontaminated photometry retains only the CM information, but not the radial one. In this sense, we used the FS-decontamination algorithm only to uncover intrinsic CMD morphologies.

4.5 Potential limitations

In principle, the present FS-decontamination method is capable of taking into account local density variations in field and cluster star sequences in CMDs (Section 4.1). To reach that goal, however, it relies on some uniformity – at least to the CMD cell scale – of statistical properties (e.g. colour and magnitude distributions), both in the offset field and in the cluster regions. Such premises may introduce some limitations to the method, basically related to photometry. Some of these are discussed below.

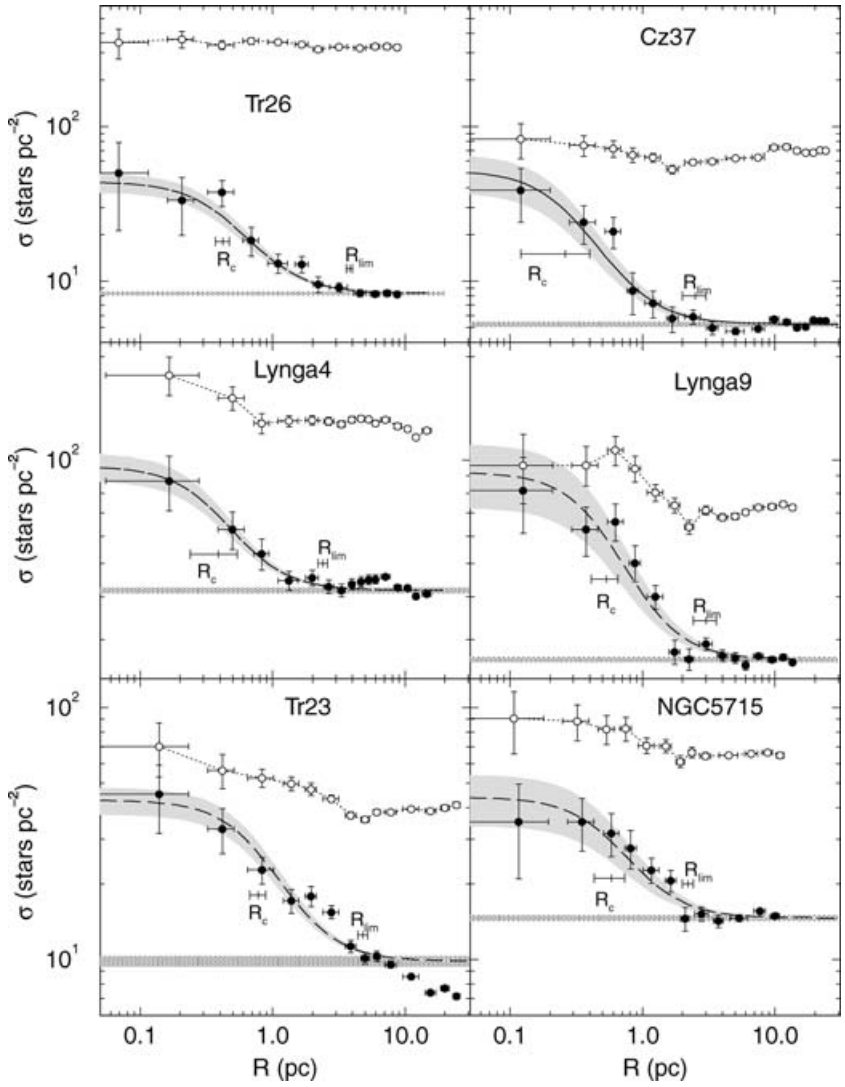

Figure 10. Radial stellar density profiles. Filled circles: colour-magnitude filtered RDPs. Dashed line: best-fitting two-parameter King profile. Horizontal shaded region: residual stellar background level measured in the comparison field. Core and limiting radii are indicated. Gray regions: standard deviation of the King fit. The striking effects of the background contamination, that produce shallow and/or disturbed profiles, are reflected in the low-contrast observed RDPs (empty circles).

(i) *Significant differential absorption.* Consider a CMD cell whose colour sides have dimensions $\Delta(J-H) = \Delta(J-K_s) = 0.2$. If the difference in absorption between cluster and offset FSs for a given cell is larger than $A_V \approx 2$ mag, the difference in colour [e.g. $(J-H)$] would be as large as the cell dimension. In that case the algorithm would assume wrong types (and possibly number) of stars as FS to be subtracted from the cell.

(ii) *Large photometric uncertainties.* Because the algorithm uses explicitly photometric errors (in terms of Gaussian probability distribution) to compute cell number density, exceedingly large uncertainties would result both in high fractions of cells with fractional numbers of stars (followed by low subtraction efficiency) and in smeared CMDs.

(iii) *Small number of cluster stars.* CMD cells of (intrinsically) poorly populated clusters inevitably suffer from small number statistics that would result in low subtraction efficiencies. In addition, the effective number of stars above the background in photometry-limited surveys falls with distance from the sun as $N^{\star}_{\rm eff} \propto 1/D_{\odot}$ (Bonatto & Bica 2005), which decreases star-count statistics of distant clusters.

(iv) *Distant and central clusters.* The main problem in these cases is the exponential growth of FS contamination with (apparent) magnitude (Section 4.3). The fraction of cluster stars in very distant and central objects may drop to a few per cent, much below the 1σ fluctuation level, especially at the 2MASS completeness limits (Section 3).

(v) *Crowding in central parts.* Rich clusters, and to some extent distant ones, may suffer from stellar crowding especially in their central regions. Angular separations smaller than $\approx$1 arcsec cannot be resolved by 2MASS. Since the offset field is less affected by crowding than clusters, FS contamination, especially for faint stars, would be overestimated.

(vi) *CMD cell dimension.* Large CMD cells might be used to minimize effects (i)–(iii), but the consequence would be a degraded CMD resolution (Section 4.1). One possible way to circumvent part of the above limitations would be to apply the FS-decontamination

algorithm on CCD photometry. Their small photometric uncertainties probably would produce less fractional numbers in cells and, thus, higher subtraction efficiencies. However, for any quantitative FS-decontamination algorithm to be efficient and statistically representative, wide surrounding fields such as those provided by 2MASS, are required. Wide fields in the optical are usually not available. The present objects do not suffer critically from the effects above.

4.6 Cluster age, reddening and distance from the Sun derived from FS-decontaminated data

Cluster age is derived with solar-metallicity Padova isochrones (Girardi et al. 2002) computed with the 2MASS J, H and K_s filters.[8] 2MASS transmission filters produced isochrones very similar to the Johnson–Kron–Cousins (e.g. Bessel & Brett 1988) ones, with differences of at most 0.01 in $(J - H)$ (Bonatto et al. 2004).

The FS-decontaminated CMD morphologies (bottom panels of Figs 5–7) provide enough constraints to derive reliable cluster ages. We derive ages in the range 0.6–1.3 Gyr, with Cz 37 being the youngest and Ly 4 the oldest cluster (column 9 of Table 1). Reddening values are in the range $E(J - H) = 0.11$–0.37 which convert to $E(B - V) = 0.35$–1.18 (column 10). Distances from the Sun are in the range $D_\odot = 1.0$–1.7 kpc (column 11). Age-solutions are plotted in the bottom panels of Figs 5–7, superimposed on the FS-decontaminated CMDs.

The present age of Tr 23 agrees with that of Carraro et al. (2006). However, they derive larger reddening [$\Delta E(B - V) \approx +0.3$] and distance from the Sun ($\Delta D_\odot \approx +0.5$ kpc). With respect to Tr 26, Kharchenko et al. (2005) found age and reddening approximately one-third of the present ones, and put the cluster approximately three times more distant.

With the recently derived value of the Sun's distance to the Galactic Centre $R_0 = 7.2$ kpc (based on updated parameters of globular clusters – Bica et al. 2006), we conclude that the present OCs are located ≈0.9–1.6 kpc inside the solar circle (column 12 of Table 1). Cz 37 is the innermost one, with Galactocentric distance $d_{GC} \approx 5.6$ kpc.

5 STRUCTURAL PARAMETERS

Structural parameters are derived by means of RDPs, defined as the projected radial distribution of the number-density of stars around the cluster centre. RDPs are built with stars selected after applying the respective CM filter (bottom panels of Figs 5–7) to the observed photometry.

5.1 Colour–magnitude filters

CM filters were previously applied in the structural analysis of the OCs M 67 (Bonatto & Bica 2003), NGC 3680 (Bonatto, Bica & Pavani 2004), NGC 188 (Bonatto, Bica & Santos 2005), NGC 6611 (Bonatto et al. 2006), NGC 4755 (Bonatto et al. 2006b), M 52 and NGC 3960 (Bonatto & Bica 2006) and the faint OCs BH 63, Lyngå 2, Lyngå 12 and King 20 (Bica et al. 2006). They are used only to discard stars with colours compatible with those of the foreground/background field. They should be wide enough to accommodate cluster MS and evolved stars colour distributions, allowing as well for the respective 1σ uncertainties. Contrary to CMD FS decontamination (Section 4), residual FSs with colours similar to those of the cluster are expected to permeate the CM filter. This residual contamination is statistically taken into account by comparisons with the offset field. Hence the need for wide surrounding fields such as those provided by 2MASS. CM filter widths account for dynamical evolution-related effects, such as enhanced fractions of binaries (and other multiple systems) towards the central parts of clusters, since such systems tend to produce a widening in the MS. Effects on CM-filter shape due to binary-induced MS widening and 2MASS photometric uncertainties have been studied in the old OC NGC 188 (Bonatto et al. 2005).

It is important to make clear that, in the context of structural and MF analyses, FS-decontaminated CMDs (bottom panels of Figs 5–7) are used exclusively to define the shape of CM-filters. They are designed to contain intrinsic cluster sequences (including as well MS-widening evolutionary effects). RDPs and MFs employ the CM-filtered observed photometry.

5.2 Radial density profiles

To avoid oversampling near the centre and undersampling at large radii, RDPs are built by counting stars in rings of increasing width with distance to the centre. The number and width of rings can be adjusted so that the resulting RDPs present good spatial resolution with moderate 1σ Poisson errors. The residual background level of each RDP corresponds to the average number of (CM-filtered) stars measured in the comparison field (Table 4).

Cluster limiting radius and uncertainty are estimated by visually comparing the RDP level (taking into account fluctuations) with the background. In this sense, R_{lim} corresponds to the distance from the cluster centre where RDP and background become statistically indistinguishable from each other (e.g. Bonatto & Bica 2005, and references therein). For practical purposes, most of the cluster stars can be considered to be contained within R_{lim}. We remark that the limiting radius should not be mistaken for the tidal radius. For instance, in populous and relatively high Galactic latitude OCs such as M 26, M 67, NGC 188 and NGC 2477, limiting radii are a factor ∼0.5–0.7 of the respective tidal radii (Bonatto & Bica 2005). The limiting radii of the present objects are given in column 7 of Table 4. It is worth remarking that tidal radii are derived from fits of King profile to RDPs, which depend on wide surrounding fields and adequate Poisson errors.

Structural parameters are derived by fitting CM-filtered RDPs with the two-parameter King (1966a) profile, which describes the central and intermediate regions of normal clusters (King 1966b; Trager, King & Djorgovski 1995). Fits were performed with a non-linear least-squares fit routine that uses errors as weights. To minimize degrees of freedom in fits, the background level (σ_{bg} – column 3 of Table 4) was kept constant, corresponding to the residual values measured in the comparison fields (Section 4). King fit parameters are the residual central density of stars (σ_{0K}) and core radius (R_{core}). Fit parameters are given in columns 4 and 6 of Table 4, and the best-fitting solutions are superimposed on the CM-filtered RDPs (Fig. 10). We quantify the background contamination by the density contrast parameter $\delta_c = \sigma_{0K}/\sigma_{bg}$ (column 5). Since δ_c is measured in CM-filtered RDPs, it does not necessarily correspond to the visual contrast produced by observed stellar distributions in XDSS images (Figs 1–3). Tr 26, for instance, presents a very low contrast both in the XDSS B image (Fig. 1) and observed RDP (Fig. 10), where $\delta_c \approx 0.1$. On the other hand, because most of the non-cluster stars have been excluded by the CM filter, the corresponding RDP presents a higher density contrast, $\delta_c \approx 4.4$.

[8] http://pleiadi.pd.astro.it/isoc_photsys.01/isoc_photsys.01.html.

Table 4. Structural parameters from CM-filtered photometry.

				RDP			MDP	
Cluster	1 arcmin (pc)	σ_{bg} (stars pc^{-2})	σ_{0K} (stars pc^{-2})	δ_c	R_{core} (pc)	R_{lim} (pc)	σ_{0K} ($M_\odot$ pc^{-2})	R_{core} (pc)
(1)	(2)	(3)	(4)	(5)	(6)	(7)	(8)	(9)
NGC 5715	0.427	14.6 ± 0.2	30 ± 10	2.1 ± 0.7	0.58 ± 0.15	2.2 ± 0.2	44 ± 12	0.67 ± 0.15
Ly 4	0.332	41.6 ± 0.2	54 ± 15	1.3 ± 0.4	0.39 ± 0.15	2.4 ± 0.2	90 ± 36	0.26 ± 0.08
Tr 23	0.553	9.9 ± 0.4	33 ± 5	3.3 ± 0.5	0.78 ± 0.11	4.8 ± 0.4	57 ± 6	0.81 ± 0.11
Ly 9	0.499	26.2 ± 0.2	66 ± 19	2.5 ± 0.7	0.53 ± 0.12	3.0 ± 0.6	113 ± 36	0.49 ± 0.12
Tr 26	0.276	8.3 ± 0.2	36 ± 6	4.4 ± 0.7	0.42 ± 0.05	4.0 ± 0.2	54 ± 17	0.45 ± 0.09
Cz 37	0.479	5.3 ± 0.1	46 ± 15	8.7 ± 2.8	0.26 ± 0.14	2.5 ± 0.5	94 ± 25	0.26 ± 0.09

Table notes. Column 2: arcmin to parsec scale. King profile is expressed as $\sigma(R) = \sigma_{bg} + \sigma_{0K}/(1 + (R/R_{core})^2)$. To minimize degrees of freedom in RDP fits, σ_{bg} was kept fixed (measured in the respective comparison fields) while σ_{0K} and R_{core} were allowed to vary. MDPs are background subtracted profiles. Column 5: cluster/background density contrast ($\delta_c = \sigma_{0K}/\sigma_{bg}$), measured in CM-filtered RDPs.

Probably because of different methods and data sets, the present values of R_{core} and R_{lim} for Tr 26 correspond to factors of 0.4 and 1.5 of those given in (Kharchenko et al. 2005). The difference, especially in R_{core}, may be attributed to their brighter limits (Kharchenko et al. 2004) producing shallower profiles for this bulge-contaminated cluster. The average values of core and limiting radii for the present objects, $\langle R_{core} \rangle = 0.47 \pm 0.14$ pc and $\langle R_{lim} \rangle = 3.0 \pm 0.9$ pc, are smaller than the corresponding ones measured in the OC sample of Schilbach et al. (2006), $\langle R_{core} \rangle = 2.0 \pm 1.3$ pc and $\langle R_{lim} \rangle = 5.0 \pm 3.2$ pc.

Fig. 10 shows RDPs of MS/evolved stars of the present objects. For absolute comparison between clusters the radius scale was converted to parsecs and the number-density of stars to stars pc^{-2} using distances derived in Section 4.6. RDPs built with observed photometry are also shown in Fig. 10. Clearly, CM-filtered profiles present less fluctuations and probe deeper into cluster structure than observed RDPs. In particular, observed profiles tend to underestimate cluster extension. Besides, CM filters were essential to unveil the cluster centroid (Section 2). Note that the RDP of Tr 23 keeps decreasing for $R \gtrsim R_{lim}$, an effect produced by the variable north–south absorption (Section 3.1).

Within uncertainties, King profile provides a good analytical representation of the stellar RDPs of the six objects, from the outer parts to the core. Since it follows from an isothermal (virialized) sphere, the close similarity of a cluster's stellar RDP with a King profile suggests that the internal structure (particularly the core) has reached some significant level of energy equipartition, which is consistent with the ages derived for these objects (Section 7).

Striking differences between observed and CM-filtered RDPs show up in Fig. 10. It is remarkable that in all cases, CM-filtered RDPs present high contrast with respect to the background and are well fitted by King profiles. On the other hand, observed RDPs are in general shallow and irregular, clearly not typical of star clusters. The photometry from which the observed RDPs were built is dominated by FS contamination, in general by a fraction larger than 90 per cent (Table 3). Accordingly, the fraction of cluster stars, with respect to that of the background, is at the 1σ level. In this sense, it should be expected that without FS decontamination (for CMD morphology) and CM-filters (for intrinsic RDPs), simple qualitative comparisons of candidate CMDs with offset fields can be misleading, especially for clusters projected in central parts of the Galaxy.

5.3 Mass density profiles

To complete the structural description of the objects we take the mass–luminosity (ML) relation derived from isochrone fits (Section 4.6) to build statistical MDPs. We follow the same systematics as that used to build RDPs. Instead of computing the number-density of stars in rings, we now assign each star a mass according to the respective ML relation. MDPs are produced by subtracting from the mass density in each ring that measured in the comparison field. They are shown in Fig. 11, together with the respective King fits. Likewise RDPs, MDPs are well described by King profiles. Core radii derived from MDPs (column 9 of Table 4) agree, at 1σ, with RDP ones (column 6).

5.4 The case of Lyngå 9

Lyngå 9 was argued to be an asterism by Carraro et al. (2005). Based on a comparison with an offset field and applying a visual method to delete FS contamination, they eliminated most MS stars, except for some at the top of the MS, and a group of bright, red stars that resembled a giant clump. They concluded that Ly 9 was not a star cluster, and that the clump could consist of a random distribution of early-type stars behind or embedded in a hypothetical obscuring cloud.

However, the present FS-decontamination algorithm (Section 4) showed statistically significant star excesses over the field that populate the giant clump and about 3 mag of the MS (bottom panel of Fig. 6). In addition, CM-filtered photometry (Section 5) produced high-contrast King-like RDP (Fig. 10) and MDPs (Fig. 11).

To further explore the scenario emerging from the FS-decontaminated CMD, we build RDPs for MS and clump stars separately. If Ly 9 is a star cluster, RDPs of both star subsamples should present similar, King-like, features. As before (Section 5.2), RDPs are built with CM-filtered photometry. The resulting MS and clump RDPs are shown in Fig. 12 (middle and bottom panels, respectively), where we show as reference the combined MS + giant clump RDP (top panel) taken from Fig. 10. Within uncertainties, both RDPs can be reproduced by similar King profiles, respectively, with $R_{core} = 0.59 \pm 0.12$ and 0.27 ± 0.12 pc. The smaller core radius of the clump RDP, as compared to that of the MS, is consistent with dynamical evolution affecting Ly 9 (Section 7), where giants are expected to be more concentrated in the cluster's central parts.

Considering that Ly 9 presents a populated MS and that its RDP, as well as that of the clump, are similar and follow a King profile, we conclude that we are dealing with an OC.

5.5 The case of Czernik 37

Carraro et al. (2005), based on $(B - V)$ and $(V - I)$ CMDs of the object (however, with no offset field for comparison) suggested

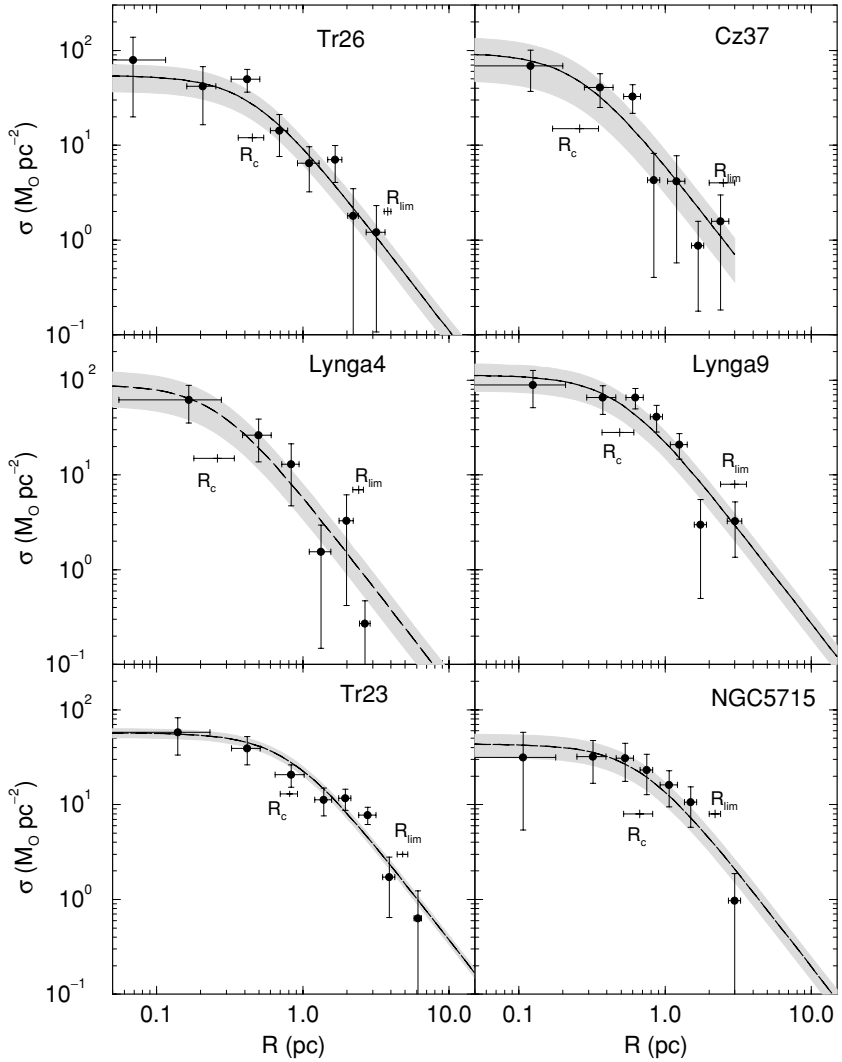

Figure 11. Similarly to RDPs (Fig. 10), background-subtracted MDPs (filled circles) are well represented by two-parameter King profiles (dashed lines) with relatively small uncertainties (shaded regions). MDPs core radii agree at 1σ with those derived from RDPs (Table 4).

that it might be a star cluster superimposed on the Galactic bulge population. It is the least-populated object of the present sample (Table 5), with an FS-decontaminated CMD featuring about 2 mag of the MS, a relatively conspicuous clump, and significant bulge star contamination (Fig. 7). However, its CM-filtered RDP is highly contrasted with the background and follows closely a King profile (Fig. 10).

We further check the OC nature of Cz 37 with RDPs built separately with (CM-filtered) MS and clump stars. The resulting MS and clump profiles (right-hand panels of Fig. 12) are similar to each other, slightly more concentrated for the clump than the MS. They follow King laws with core radii $R_{\rm core} = 0.32 \pm 0.10$ and 0.22 ± 0.10 pc, respectively, for the MS and clump RDPs. Accordingly, Cz 37 is confirmed to be an OC.

5.6 Model OCs projected on varying backgrounds

Different luminosity functions detected in central parts of most star clusters, as compared to the field, may provide a means from which these objects can identified in plate materials. However, in the context of this work, structural parameters are derived from number-density profiles that consider only the number of stars in rings, regardless of magnitude. In short, the issue here is not star cluster identification, but to measure core and limiting radii from RDPs of objects subject to different amounts of background contamination.

To further explore the OC structural description we test the effect of a varying background level on measurements of cluster core and limiting radii. Since determination of $R_{\rm lim}$ depends directly on the ability to see where the RDPs become indistinguishable from the background level, it is expected that measurements of non-populous OCs, especially those projected against central parts of the Galaxy, will be underestimated.

King-like OCs are simulated with (projected) stellar radial number-density profiles given by $\sigma(R) = \sigma_{\rm bg} + \sigma_{0K}/(1 + (R/R_{\rm core})^2)$. We define the cluster/background contrast parameter as $\delta_c = \sigma_{0K}/\sigma_{\rm bg}$. Model OCs contain 350 equal-mass stars distributed in a region with a structure described by $R_{\rm core} = 0.4$ pc and $R_{\rm lim} = 4.0$ pc, representative values of the OCs dealt with in this work (Table 4). (x, y) coordinates of the test-stars are randomly selected with a probability proportional to King profile's number density at position $R = \sqrt{x^2 + y^2}$, in steps of $\Delta R = 0.01$ pc, in order to preserve the spatial resolution of the analytical profile. To

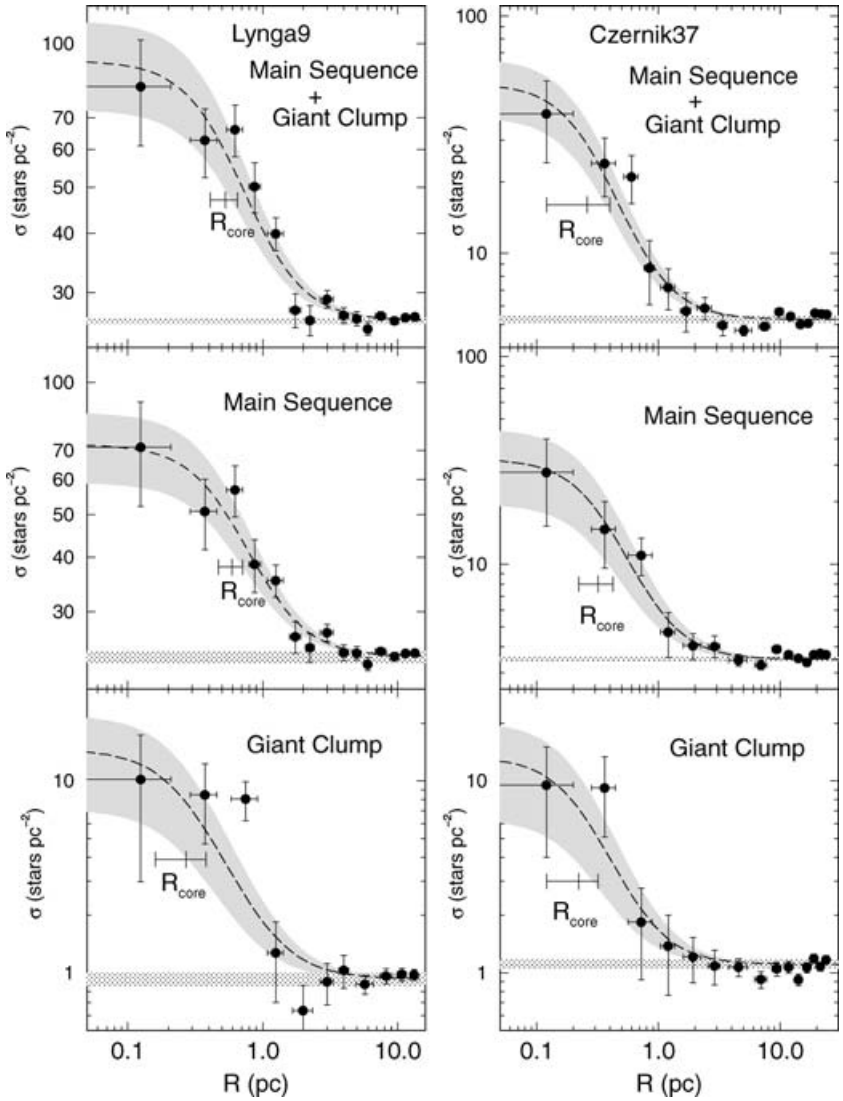

Figure 12. RDPs of Ly 9 (left panels) and Cz 37 (right panels) built with CM-filtered photometry for different magnitude ranges. Top panels: full magnitude range, i.e. MS + giant clump stars. Middle panels: MS stars. Bottom panels: Giant clump stars. Symbols as in Fig. 10.

Table 5. Parameters related to mass functions and dynamical states.

	Evolved			Observed MS			Evolved + Extrapolated MS				
Cluster	N^* (stars)	m ($M_\odot$)	Δm ($M_\odot$)	χ	N^* (stars)	M_{obs} ($M_\odot$)	N^* (10^2stars)	M_{OC} (10^2 $M_\odot$)	σ ($M_\odot$ pc^{-2})	ρ ($M_\odot$ pc^{-3})	τ
(1)	(2)	(3)	(4)	(5)	(6)	(7)	(8)	(9)	(10)	(11)	(12)
NGC 5715	8 ± 2	18 ± 6	1.1–2.2	1.3 ± 0.5	93 ± 23	145 ± 20	20 ± 15	7.3 ± 3.1	48 ± 21	16 ± 7	35 ± 25
Ly 4	3 ± 1	7 ± 2	1.0–1.9	1.3 ± 0.2	105 ± 40	130 ± 30	22 ± 16	7.6 ± 3.0	42 ± 17	13 ± 5	41 ± 28
Tr 23	16 ± 9	35 ± 20	1.0–2.1	1.4 ± 0.6	300 ± 40	483 ± 42	86 ± 67	31 ± 13	43 ± 18	6.7 ± 2.8	4.9 ± 3.5
Ly 9	37 ± 7	73 ± 15	1.1–1.9	1.1 ± 0.7	124 ± 32	213 ± 37	26 ± 22	10 ± 5	37 ± 17	9.2 ± 4.1	18 ± 14
Tr 26	21 ± 5	42 ± 10	1.1–2.3	1.7 ± 0.6	100 ± 31	150 ± 24	24 ± 18	8.7 ± 3.5	17 ± 7	3.3 ± 1.3	15 ± 10
Cz 37	17 ± 5	44 ± 13	1.8–2.5	-1.1 ± 0.9	41 ± 14	89 ± 19	1.4 ± 0.7	2.1 ± 1.0	11 ± 5	3.2 ± 1.6	196 ± 88

Table notes. Column 4: effective mass range of the observed MS. Column 7: stellar mass of the observed MS. Column 9: mass extrapolated to 0.08 $M_\odot$. Column 12: dynamical-evolution parameter $\tau = \text{age}/t_{rel}$.

avoid small number statistics at inner regions (the small ring-areas may contain fractions of stars), we run 100 simulations and take the average probability at each position to build the final RDPs.

The spatial distribution of stars of the background-free OC is shown in Fig. 13 (top left-hand panel), where the core and halo subsystems are clearly visible. To this OC we add backgrounds with $\delta_c = 10$ (top right-hand panel), 3.3 (bottom left-hand panel) and 2 (bottom right-hand panel). As expected, only the (equal-mass star) core detaches from the stellar distributions with increasing background level. The picture does not change much in real star

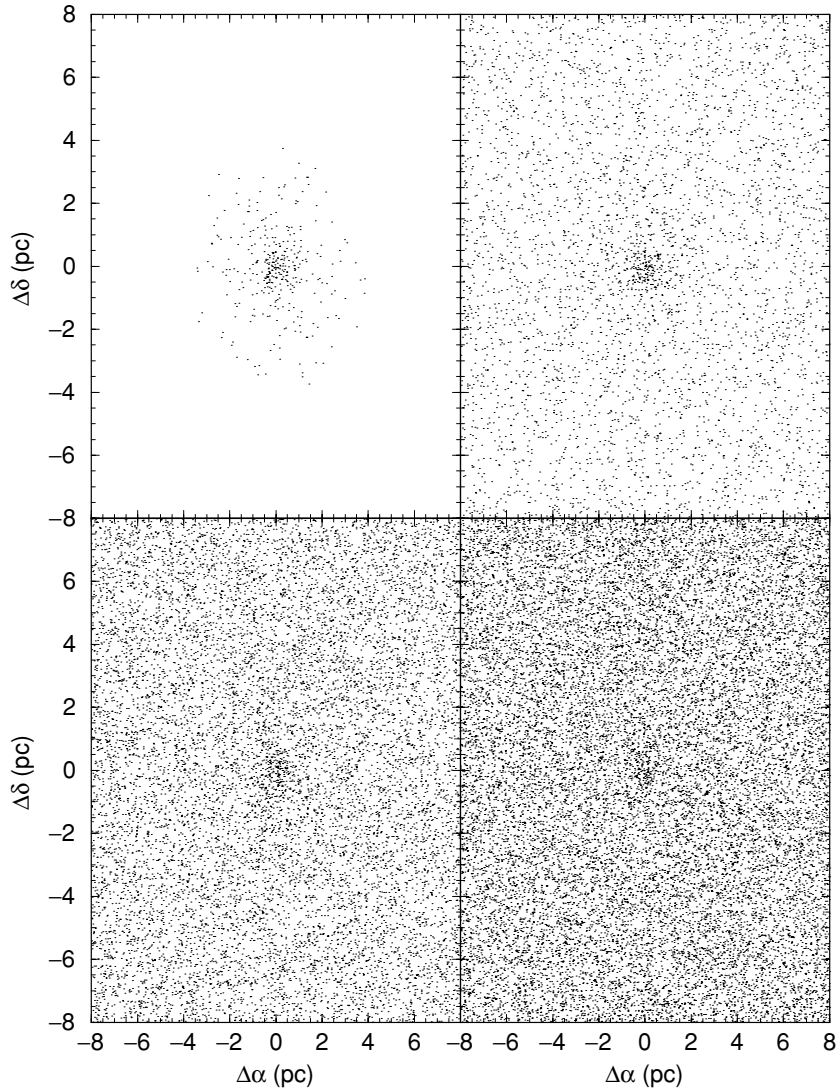

Figure 13. Visual contrast produced by a model (King profile) OC described by $R_{\rm core} = 0.4$ pc, $R_{\rm lim} = 4.0$ pc and 350 member stars projected against backgrounds with varying density levels ($\delta_{\rm c} = \sigma_{0\rm K}/\sigma_{\rm bg}$). Top-left panel: no background. Top-right: $\delta_{\rm c} = 10$. Bottom-left: $\delta_{\rm c} = 3.3$. Bottom-right: $\delta_{\rm c} = 2$.

clusters, since bright stars in these objects tend to be concentrated in or near the core. As a consequence of low surface brightness, the stellar distribution of the cluster halo, especially in the outer parts, is not much different from that of the field.

The corresponding model-OC RDPs are shown in Fig. 14, together with the King fits and background levels. RDPs are built with a similar ring-width distribution to that used for the RDPs and MDPs in Figs 10 and 13, respectively. As expected, core radii derived from King fits do not depend on $\delta_{\rm c}$. Limiting radii, on the other hand decrease with increasing $\delta_{\rm c}$, changing from $R_{\rm lim} = 4.0 \pm 0.5$ (background-free) to $R_{\rm lim} = 3.5 \pm 0.5$ for $\delta_{\rm c} = 2$, a $\sim$10 per cent factor.

As a caveat we note that the backgrounds used in the simulations are spatially uniform, subject only to 1σ Poisson fluctuations in RDPs. Galactic backgrounds present higher spatial fluctuations (e.g. Figs 1–3) associated with e.g. differential absorption and local FS enhancements that tend to produce additional decrease in limiting radii. Thus, we expect to measure limiting radii about 10–20 per cent smaller than intrinsic ones in OCs containing a few hundred stars projected against central parts of the Galaxy. Obviously, OCs less populous than those simulated here are expected to be significantly more affected by low contrast, to the point that most may not be observed at all (Bonatto et al. 2006a).

6 MASS DETERMINATIONS

6.1 Mass function slopes

In previous sections we presented strong evidence, in terms of CMDs, RDPs and MDPs, that the six objects dealt with in this work are intermediate-age OCs. Based on this we build MFs and compute stellar masses using CM-filtered photometry (Section 5), that increases statistical significance and cluster membership probability.

The methods presented in Bonatto & Bica (2005) (and references therein) are used to derive MFs, $[\phi(m) = \frac{{\rm d}N}{{\rm d}m}]$. We build them using the three 2MASS bands separately, and the ML relations obtained from the respective Padova isochrones and distances from the Sun (Section 3). The effective magnitude range over which MFs are computed is that where clusters present an excess of stars with

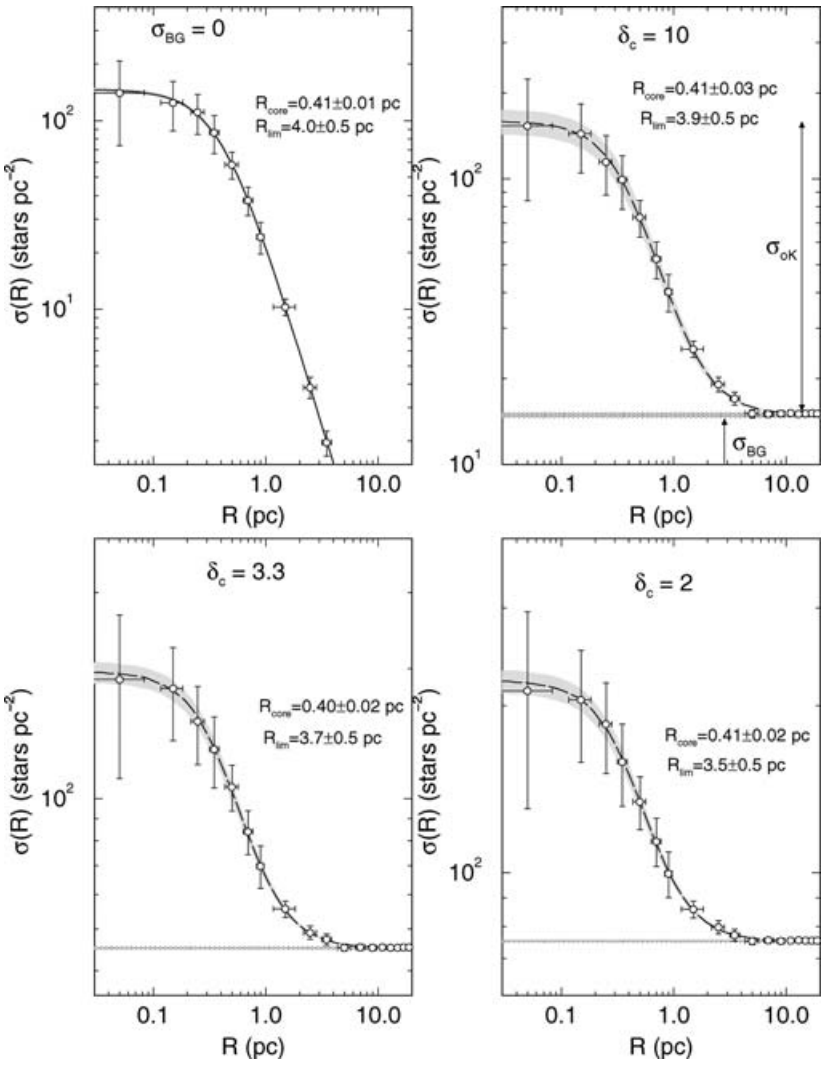

Figure 14. RDPs of the model OCs shown in Fig. 13. Limiting radius tends to be underestimated as the density contrast parameter drops. Panels follow the same order of δ_c as in Fig. 13. Core (from King fit) and limiting radii (from RDPs) are indicated. For visualization purposes, vertical scales are different in each panel.

respect to the comparison field. In all cases it begins right below the TO and ends at a faint-magnitude limit brighter than that stipulated by the 2MASS completeness limit (Section 3). The effective magnitude ranges of the present OCs are shown as the shaded areas in the bottom panels of Figs 5–7; the corresponding stellar mass ranges are given in column 4 of Table 5. Further details on MF construction are given in Bica et al. (2006).

The resulting MFs cover significant mass ranges, typically from 1 to 2.5 $M_\odot$. They are shown in Fig. 15, where fits with the function $\phi(m) \propto m^{-(1+\chi)}$ are included; MF slopes are given in column 5 of Table 5. The error bars basically reflect the significant number of stars present in the MS. Within uncertainties, the MFs of NGC 5715, Ly 4, Tr 23, Ly 9 and Tr 26 have slopes similar to that of Salpeter (1955) initial mass function (IMF) ($\chi = 1.35$). Cz 37, on the other hand, presents a flat MF which may result from an advanced dynamical state (Section 7).

6.2 Cluster mass

Table 5 gives parameters of the target clusters measured in the CMDs and derived from MFs. The number of evolved stars (column 2) was obtained by integration of the (background-subtracted) CM-filtered luminosity function for stars brighter than the TO. Multiplying this number by the stellar mass at the TO yields an estimate of the mass stored in evolved stars (column 3). The number and mass of the observed MS stars (columns 6 and 7, respectively) were derived by integrating the MFs over the effective MS mass ranges (column 4).

To estimate the total stellar mass we extrapolate the observed MFs down to the H-burning mass limit (0.08 $M_\odot$). For masses below the present detection threshold (Table 4) we rely the extrapolation on Kroupa (2001) universal IMF, in which $\chi = 0.3 \pm 0.5$ for the range $0.08 \leqslant m(M_\odot) \leqslant 0.5$ and $\chi = 1.3 \pm 0.3$ for $0.5 \leqslant m(M_\odot) \leqslant 1.0$. In the cases where the present MF slopes are flatter than or similar (within uncertainties) to Kroupa's, we adopt the measured values of χ. The total (extrapolated MS + evolved) values of number, mass, projected and volume densities are given in columns 8–11 of Table 5.

The number of MS and evolved member stars ranges from ≈58 to ≈316. As already indicated by the small number of probable member stars present in the FS-decontaminated CMD (Fig. 7), the least populous OC is Cz 37. The corresponding mass of the MS and evolved stars is in the range $130 \lesssim M_{obs}(M_\odot) \lesssim 520$, while the extrapolated masses are a factor ∼4.5–6 times larger than the

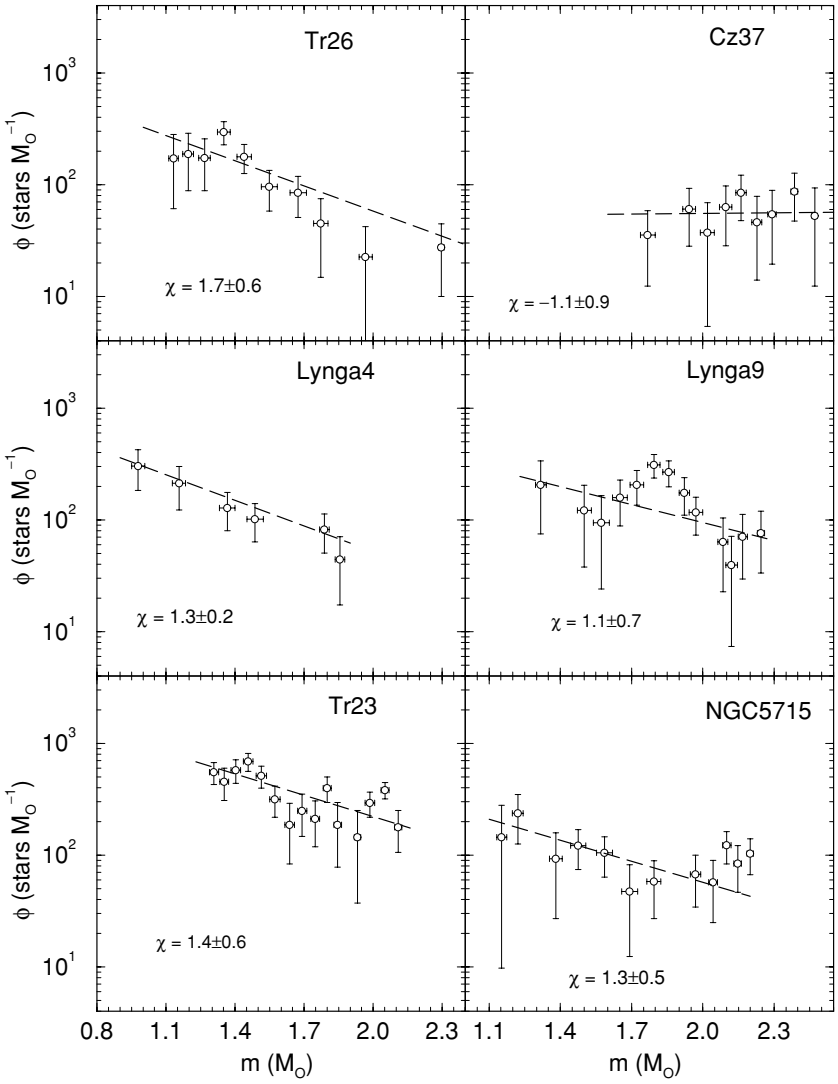

Figure 15. 2MASS mass functions fitted with $\phi(m) \propto m^{-(1+\chi)}$. Except for Cz 37, the remaining OCs have MF slopes similar to Salpeter's IMF.

observed ones, except for Cz 37, which is only about twice as large, again consistent with its CMD morphology.

As a caveat we note that the total mass estimates should be taken as upper limits, since because of dynamical evolution, significant fractions of the low-mass content may have been lost to the field, especially in the case of Cz 37 (Section 7), as reflected in the flat MF.

7 DISCUSSION

Star clusters form in collapsing molecular clouds in which variable fractions (10–60 per cent) of the parent gas are converted into stars. They remain embedded in the clouds for about 2–5 Myr (e.g. Lada & Lada 2003), and their dynamical state at that early phase can be described as out of virial equilibrium (e.g. de la Fuente Marcos & de la Fuente Marcos 2002). Following the rapid expulsion of the unused gas by massive winds and supernovae, stars end up with excessive velocities with respect to the new, decreased, potential (e.g. Boily & Kroupa 2002; de la Fuente Marcos & de la Fuente Marcos 2002). As a consequence, clusters grow in all scales as they reach for virialization. *N*-body simulations of massive star clusters (e.g. Goodwin & Bastian 2006) show that after a few 10^7 yr, core growth levels off as some energy equipartition is reached, a phase that is followed by a decrease in core size. The outer parts, on the other hand, keep increasing in size. At some point, the intrinsic cluster size may no longer be observable because of the increased volume and low number-density of cluster stars at large radii. The external parts may become indistinguishable from the background, particularly for clusters projected against the central parts of the Galaxy (e.g. Bonatto et al. 2006a). Besides, interactions with the disc and the tidal pull of the Galactic Centre/bulge, as well as collisions with molecular clouds, tend to destroy poorly populated OCs in a timescale of a few 10^8 Myr (Bergond, Leon & Guibert 2001), especially for centrally located OCs. Although conceptually different, these effects combine to produce observable changes in cluster structural parameters. For the outer parts of poorly populated and centrally located OCs the following are expected. (i) Cluster expansion due to dynamical evolution; (ii) decrease in cluster/background contrast especially for $R \rightarrow R_{\rm lim}$; and (iii) enhanced disruption rates.

Empirical determinations of cluster limiting radii depend critically on RDP and background levels (and respective fluctuations). Thus, effects (i) and (ii) should affect more $R_{\rm lim}$ than $R_{\rm core}$, since

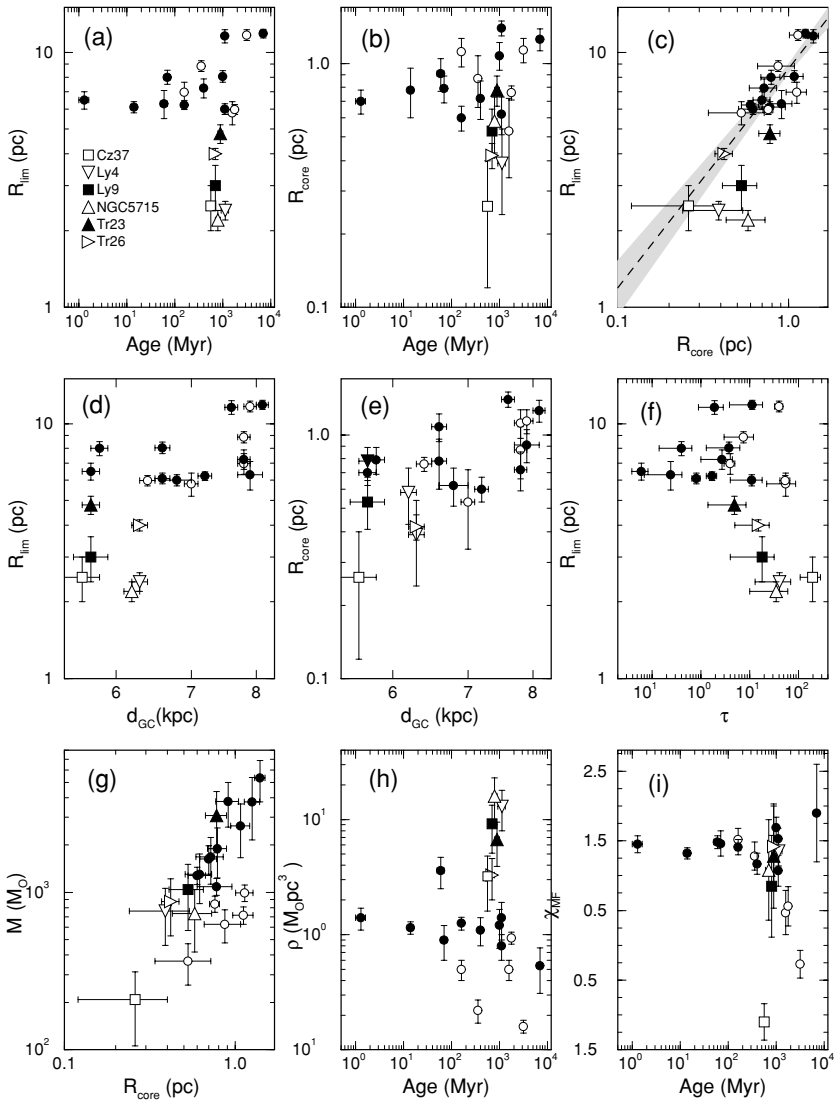

Figure 16. Relations involving structural and dynamical state parameters of OCs. Filled symbols: OCs more massive than 1000 $M_\odot$. Empty symbols: less massive OCs.

the latter is derived by fitting an analytical function to the distribution of points provided by the RDP, as indicated by model-cluster simulations (Section 5.6). On the other hand, dynamical evolution may accelerate because of (iii), thus increasing the rate of large scale core-halo mass segregation and low-mass star evaporation to the field – effects that tend to increase intrinsic cluster size and decrease $R_{\rm core}$. Since mass segregation drives preferentially low-mass stars to the outer parts of clusters, cluster/background contrast in these regions tends to lower as clusters age. As an observational consequence, smaller values of limiting radii should be measured, especially for clusters in dense fields.

To disentangle these effects we employ a set of parameters that probe structure and dynamical state derived for a sample of nearby OCs with ages in the range 70–7000 Myr and masses within 400–5300 $M_\odot$, following most of the present methodology (Bonatto & Bica 2005). To the original reference sample were added NGC 6611 (Bonatto et al. 2006) and NGC 4755 (Bonatto et al. 2006b). Clusters are differentiated according to total mass (smaller or larger than 1000 $M_\odot$). The evolutionary parameter $\tau = {\rm age}/t_{\rm rel}$ (column 12 of Table 5), where $t_{\rm rel}$ is the relaxation time (Binney & Tremaine 1987), was found to be a good tracer of dynamical states. In particular, significant flattening in cluster MF slopes due to dynamical effects such as mass segregation is expected to occur for $\tau \gtrsim 7$. Details on parameter correlation in the reference sample are given in Bonatto & Bica (2005).

In panels (a) and (b) of Fig. 16 we compare core and limiting radii of the present OCs with those of the reference sample in terms of cluster age. In all cases, both kinds of radii appear to be significantly smaller than those of nearby OCs of similar ages, especially in limiting radius. Tr 23 and Tr 26 have $R_{\rm lim} \sim 1/2$ of those in the reference sample, while for the remaining ones $R_{\rm lim} \sim 1/3$. A similar effect occurs for Galactocentric distances (panels d and e). Core and limiting radii in the reference sample are related by $R_{\rm lim} = (8.9 \pm 0.3) \times R_{\rm core}^{(1.0\pm0.1)}$ (panel c), which suggests that both kinds of radii undergo a similar scaling, at least for $0.5 \lesssim R_{\rm core}({\rm pc}) \lesssim 1.5$ and $5 \lesssim R_{\rm lim}({\rm pc}) \lesssim 15$. Except for Cz 37 and Tr 26, the remaining OCs do not follow that relation. Considering that we may have underestimated $R_{\rm lim}$ by 10–20 per cent (Section 5.6), this again suggests that the present OCs are either intrinsically small or have been suffering important evaporation effects. The dependence of $R_{\rm lim}$ on evolutionary

parameter τ (panel f) supports this conclusion, since except for Tr 23, the remaining OCs have τ significantly larger than 7 (Bonatto & Bica 2005).

Relations presented in the bottom panels of Fig. 16 also indicate that we are dealing with OCs affected by tidal and low-contrast effects, especially in their outer parts. The relation of their (total) masses with core radii is consistent with that defined by nearby OCs (panel g), in both mass regimes. Mass density, on the other hand, that in the context of this work is basically sensitive to limiting radius, seems to be exceedingly high with respect to nearby OCs. Except for Cz 37 and Tr 26, the remaining OCs have a mass density $\sim$8 times higher than that of nearby OCs. If mass values are reasonably well determined, as suggested by panel (g), a factor of $\sim$2 applied to their limiting radii would bring densities close to the typical values of nearby OCs. Interestingly, this correction would as well put the deviant OCs back into the tight core and limiting radii relation (panel c). Even so, they would still have core and limiting radii smaller than those of nearby OCs, with $R_{\rm core} \lesssim 0.6$ pc and $R_{\rm lim} \lesssim 5.2$ pc. Considering the discussion presented in Section 5.6, most of the smaller limiting radii can be accounted for by dynamical effects, both internal and external to the clusters.

Probably because of its innermost position in the Galaxy (Table 1) and low mass (Table 5), Cz 37 seems to be the OC most affected by tidal effects (and accelerated dynamical evolution), since it shows the flattest MF slope (panel i), smallest core radius and total mass in the present sample.

8 SUMMARY AND CONCLUSIONS

Low-contrast star clusters projected against central parts of the Galaxy present a challenge to observational projects that intend to improve their census and derive fundamental and dynamical parameters. High background levels may not allow detection of the external parts of clusters, because of low surface brightness. In many cases, it may not be possible to detect faint clusters above the background at all (e.g. Bonatto et al. 2006a).

Theoretical predictions indicate that poorly populated OCs must by far be the majority of the star cluster population in the Galaxy. Indeed, Bonatto et al. (2006a) have found that the distribution function for the number of OCs with η observed member stars (considering all disc directions in the Galaxy) follows $\phi_{\rm OC}(\eta) = \frac{{\rm d}N_{\rm OC}}{{\rm d}\eta} \propto {\rm e}^{-\eta/95}$. This implies that the fraction of Milky Way OCs with $\eta \lesssim 100$ observed member stars amounts to about 65 per cent, while for $\eta \lesssim 300$ it increases to $\sim$96 per cent. Derivation of accurate fundamental and structural parameters of poorly populated OCs, especially those inside the solar circle, is important as well to test models of cluster tidal disruption.

In this work a set of tools were applied – for example, FS decontamination, CM filter and diagnostic-diagrams for structure and dynamical state – to six OCs projected not far from the Galactic Centre. The objects are NGC 5715, Ly 4, Ly 9, Tr 23, Tr 26 and Cz 37, whose near-IR CMDs are heavily contaminated by FSs, especially bulge ones. Probably because of this, these objects could not previously be studied in detail. Ly 9, in particular, was considered to be a fluctuation of the dense field (Carraro et al. 2005). We work with wide-field extractions of 2MASS photometry.

2MASS field-star decontaminated and CM-filtered photometry produced compelling evidence – in terms of CMDs with well-defined cluster sequences and stellar density profiles following King law – that the six objects are OCs about the Hyades age [$0.6 \lesssim$ age(Gyr) $\lesssim 1.3$] located 0.9–1.6 kpc inside the solar circle. In all cases core, and especially limiting radii, appear to be smaller than those of nearby OCs outside the solar circle. We measured $0.26 \lesssim R_{\rm core}({\rm pc}) \lesssim 0.66$ and $2.2 \lesssim R_{\rm lim}({\rm pc}) \lesssim 4.4$.

Simulations of King-like OCs have shown that high background levels may have affected limiting radius estimates for the present OCs, in the sense that $R_{\rm lim}$ can be underestimated by about 10–20 per cent. $R_{\rm core}$, on the other hand, is almost insensitive to the range of background levels used in the simulations. Thus, background contamination alone cannot account for the small limiting radii measured in the present OCs, which are scaled down by factors of 1/3–1/2, as compared to a sample of nearby OCs. Except for Cz 37 which has a flat MF, the remaining OCs have Salpeter-like MFs, within uncertainties. Mass stored in observed MS and evolved stars amounts to $130 \lesssim M_{\rm obs}({\rm M}_\odot) \lesssim 520$. Total masses, estimated by extrapolation of the MFs to 0.08 $\rm M_\odot$, are in the range $210 \lesssim M_{\rm OC}({\rm M}_\odot) \lesssim 2700$. However, we point out that total mass estimates may be upper limits because of dynamical evolution effects.

With the help of diagnostic diagrams that probe structure and dynamical state of OCs, we find evidence that the 6 objects have been suffering significant tidal effects (for ages older than $\sim$600 Myr). Such tidal effects may have accelerated their dynamical evolution, especially in Cz 37, the innermost OC of the present sample with a flat MF. Large-scale mass segregation and low-mass star evaporation drive preferentially faint stars to large distances from the cluster centre. However, because dynamically inflated cluster external regions end up having a low surface brightness, they tend to become indistinguishable from the background when projected against dense stellar fields. As an observational consequence of these effects, poorly populated OCs projected against the central parts of the Galaxy tend to have smaller limiting radii than those measured in similar OCs located at high Galactic latitudes and/or far from the centre.

Arguments based only on observed CMD morphology may not be enough to establish the nature of objects in dense fields as star clusters. Instead, this work shows that stronger constraints are provided by FS-decontaminated CMDs and the shape of CM-filtered RDPs, especially when RDPs of different magnitude domains present similar features. Besides, with the quantitative tools we have been developing in this series of works, it is becoming feasible to explore faint OCs in dense stellar fields with 2MASS photometry, provided care is taken to statistically identify probable member stars (to better define cluster stellar sequences on CMDs) and exclude stars with discordant colours (for more intrinsic cluster RDPs and MFs). Considering as well structure and dynamical state diagnostic-diagrams, it is becoming possible to disentangle high background levels from tidal effects in the outer parts of OCs.

ACKNOWLEDGMENTS

We thank an anonymous referee for helpful suggestions. This publication makes use of data products from 2MASS, which is a joint project of the University of Massachusetts and the Infrared Processing and Analysis Centre/California Institute of Technology, funded by the National Aeronautics and Space Administration and the National Science Foundation. This research has made use of the WEBDA data base, operated at the Institute for Astronomy of the University of Vienna. We acknowledge support from the Brazilian Institution CNPq.

REFERENCES

Alter G., Balazs B., Ruprecht J., Vanysek J., 1970, Catalogue of Star Clusters and Associations, 2nd edn. Akademiai Kiado, Budapest

Bertelli G., Nasi E., Girardi L., Chiosi C., Zoccali M., Gallart C., 2003, AJ, 125, 770
van den Bergh S., Hagen G. L., 1975, AJ, 80, 11
Bergond G., Leon S., Guibert J., 2001, A&A, 377, 462
Bessel M. S., Brett J. M., 1988, PASP, 100, 1134
Bica E., Bonatto C., 2005, A&A, 443, 465
Bica E., Bonatto C., Dutra C. M., 2003, A&A, 405, 991
Bica E., Bonatto C., Dutra C. M., 2004, A&A, 422, 555
Bica E., Bonatto C., Blumberg R., 2006, A&A, 460, 83
Bica E., Bonatto C., Barbuy B., Ortolani S., 2006, A&A, 450, 105
Binney J., Tremaine S., 1987, Galactic Dynamics. Princeton Univ. Press, Princeton, NJ
Boily C., Kroupa P., 2002, in Grebel E., Brandner W., eds, ASP Conf. Ser. Vol. 285, Modes of Star Formation and the Origin of Field Populations. Astron. Soc. Pac., San Francisco, p. 141
Bonatto C., Bica E., 2003, A&A, 405, 525
Bonatto C., Bica E., 2005, A&A, 437, 483
Bonatto C., Bica E., 2006, A&A, 455, 931
Bonatto C., Santos J. F. C., Jr, Bica E., 2006, A&A, 445, 567
Bonatto C., Bica E., Girardi L., 2004, A&A, 415, 571
Bonatto C., Bica E., Pavani D. B., 2004, A&A, 427, 485
Bonatto C., Bica E., Santos J. F. C., Jr, 2005, A&A, 433, 917.
Bonatto C., Kerber L. O., Bica E., Santiago B. X., 2006a, A&A, 446, 121
Bonatto C., Bica E., Ortolani S., Barbuy B., 2006b, A&A, 453, 121
Carraro G., Janes K. A., Eastman J. D., 2005, MNRAS, 364, 179
Carraro G., Janes K. A., Costa E., Méndez R. A., 2006, MNRAS, 368, 1078
Dias W. S., Assafin M., Flório V., Alessi B. S., Líbero V., 2006, A&A, 446, 949
Dutra C. M., Santiago B. X., Bica E., 2002, A&A, 383, 219
Friel E. D., 1995, ARA&A, 33, 38
de la Fuente Marcos R., de la Fuente Marcos C., 2002, Ap&SS, 280, 381
Girardi L., Bertelli G., Bressan A., Chiosi C., Groenewegen M. A. T., Marigo P., Salasnich B., Weiss A., 2002, A&A, 391, 195
Goodwin S. P., Bastian N., 2006, MNRAS, 373, 752
Janes K. A., Phelps R. L., 1994, AJ, 108, 1773
Kharchenko N. V., Piskunov A. E., Röser S., Schilbach E., Scholz R.-D., 2004, AN, 325, 740
Kharchenko N. V., Piskunov A. E., Röser S., Schilbach E., Scholz R.-D., 2005, A&A, 438, 1163
King I., 1966a, AJ, 71, 64
King I., 1966b, AJ, 71, 276
Kroupa P., 2001, MNRAS, 322, 231
Lada C. J., Lada E. A., 2003, ARA&A, 41, 57
Lauberts A., 1982, ESO/Uppsala Survey of the ESO(B) Atlas. European Southern Observatory, Garching
Lyngå G., 1982, A&A, 109, 213
Lyngå G., 1985, IAUS, 106, 143
Moffat A. F. J., Vogt N., 1975, A&AS, 20, 155
Piskunov A. E., Kharchenko N. V., Röser S., Schilbach E., Scholz R.-D., 2006, A&A, 445, 545
Ruprecht J., 1966, Bull. Astron. Inst. Czech., 17, 33
Salpeter E., 1955, ApJ, 121, 161
Schilbach E., Kharchenko N. V., Piskunov A. E., Röser S., Scholz R.-D., 2006, A&A, 456, 523
Skrutskie M. F. et al., 1997, in Garzon F., Epchtein N., Omont A., Burton B., Persei P., eds, The Impact of Large Scale Near-IR Sky Surveys. Kluwer, Netherlands
Soares J. B., Bica E., 2002, A&A, 388, 172
Trager S. C., King I. R., Djorgovski S., 1995, AJ, 109, 218

This paper has been typeset from a TEX/LATEX file prepared by the author.